An Assessment of Reverse Electrodialysis for Application to Small-Scale Aquatic Systems

by

Marc C. Samland

B.S. Mechanical Engineering
United States Military Academy, 2016

Submitted to the
Department of Mechanical Engineering
in Partial Fulfillment of the Requirements for the Degree of

Master of Science in Mechanical Engineering
at the
Massachusetts Institute of Technology

June 2018

Signature of Author: _____

Department of Mechanical Engineering
May 25, 2018

Certified by: _____

Douglas P. Hart
Professor of Mechanical Engineering
Thesis Supervisor

Accepted by: _____

Rohan Abeyaratne
Professor of Mechanical Engineering
Chairman, Committee for Graduate Students

THIS PAGE INTENTIONALLY LEFT BLANK

An Assessment of Reverse Electrodialysis for Application to Small-Scale Aquatic Systems

by

Marc C. Samland

Submitted to the Department of Mechanical Engineering
on May 25, 2018 in Partial Fulfillment of the
Requirements for the Degree of

Master of Science in Mechanical Engineering

ABSTRACT

Reverse electrodialysis (RED) is a means by which to produce electrical power through the flow of Na^+ and Cl^- ions from seawater to fresh water across ion selective membranes. While current research has largely focused on utilizing RED for large-scale commercial power, this thesis explores the feasibility of using RED as a power source for remote sensing devices and unmanned underwater vehicles, with a specific focus on the Arctic Ocean. A parameter sweep is developed using MATLAB in order to estimate the ideal dimensions and flow rates for an RED stack with respect to its volumetric power density. Unlike previous models, this model accounts for considerations unique to RED's application to unmanned underwater vehicles and remote sensing devices in variable environmental conditions. The model maintains broad generality for use with a variety of RED design configurations, while also demonstrating agreement with empirical data collected from specific experimental tests. The computational model is validated by empirical data from three previous studies and used to find a specific and volumetric power density for RED of 2.35 W/kg and 206×10^{-3} W/cm^3 at 298K with salt concentrations of 0.7 and 35 g NaCl/ kg H_2O. This thesis then compares RED to other environmental energy harvesting systems and determines RED to be a competitive power source within the environmental constraints of the Artic. Regarding the use of RED as a secondary power source to charge lithium ion batteries, it is found that it would require an RED stack over four days to recharge a lithium ion battery of equal mass and over thirteen days for a battery of equal volume. For use with low power systems requiring constant power, an RED stack could supply more power than a lithium ion battery of equivalent mass for durations longer than three days and ten days for one of equivalent volume.

Thesis Supervisor: Douglas P. Hart
Title: Professor of Mechanical Engineering

THIS PAGE INTENTIONALLY LEFT BLANK

Acknowledgments

I would like to thank all my friends and family for their encouragement and constant support in the midst of this endeavor! Without you I am certain that I never would have come this far. Your love and friendship have helped me persevere as I have been molded into the officer and engineer that I am today.

To my parents, Jim and Debbie, you guys have always been a source of encouragement and wisdom, even when I didn't care for it at the time. Thank you for your unconditional love and support through thick and thin. You have always been there to help me achieve my dreams from attending USMA to now studying at MIT. Dad, I owe you special thanks for acting as the ultimate grammar check for all of my written work. Your last minute proofreading has been such a boon during my academic career!

To my siblings, Alex and Anna, your encouragement never ceases to put a smile on my face. You continue to play a huge role in my life, even as we are scattered across the world.

To Chris Swanson and Chris Lawson, the instrumentality of your discipleship and mentorship on my life here at MIT cannot be adequately expressed in words. You have made my learning experience at MIT so much more than merely academic, teaching me how godly men navigate life. I hope I can emulate the character and steadfastness that you have shown me.

To Eric Morgan, thank you for your mentorship and guidance these past two years. I'm certain that without your encouragement, guidance, and understanding in the midst of difficult times that I would never have made it. My only regret is that I never got to writing this thesis in LaTeX for you.

To Doug Hart, thank you for adopting me into your lab family and for teaching me all about the world of academia. Your insight and stories taught me so much! Thank you again for your flexibility in helping me to finish this thesis.

To all of those in Doug's Fun House, thank you for making the lab a fun place to be and for all your advice and insight over the last two years. To Mark, I never get tired of hearing about your adventures around the globe. Maybe one day I will even catch up to your country count. To Brandon, your help and patience with my research can't be quantified. To Thanasi, thank you for your mentorship and not blinding me with your laser. To Alban, without you our lab group would be a mess. To Peter, I wish I could cross match my socks and spend Doug's money as well as you. To Jason, I hope your enthusiasm for research never fades! Finally, to that old Annapolis grad, thank you for teaching me the ropes of how to survive MIT as an Academy grad. Too bad Navy can't seem to pull it together… *Go Army, Beat Navy!*

To Vicki Dydek and the members of Group 73 at Lincoln Laboratory, thank you for your assistance these past two years. Your feedback, advice, and support have played a significant role in making this research possible.

To Jason Vincent, and Jake, you guys introduced me to MIT and ensured I stuck around with Cru. Your friendship has been huge and I've missed you guys. To Jasper and Rich, you guys have helped me survive these past two years, holding me accountable and devising activities to give me a break from research. Your loyal friendship has meant a lot. Finally, to SWAT, I love you guys and can't wait to hear about the impact you'll make these next few years.

Soli Deo Gloria.

THIS PAGE INTENTIONALLY LEFT BLANK

Contents

List of Figures

10

List of Tables

THIS PAGE INTENTIONALLY LEFT BLANK

Chapter 1
Introduction and Background

One form of renewable energy that has received increased interest due to its enormous untapped potential is salinity gradient power (SGP), which is the controlled Gibbs free energy of mixing between two water sources of differing salt concentrations. This mixing occurs naturally at river estuaries, beneath icebergs, and along the ocean's surface following heavy rainfall, but the energy is often dissipated as entropy. This represents wasted chemical energy, which is released during this mixing process. The energy released is equivalent to the kinetic energy of an equal mass of water falling from a 270m waterfall, with an energy density of 0.81 kWh/m^3 of water [1]. It has been estimated that the global theoretical potential of SGP is 1.4-2.6 TW, of which 60% is thought to be harvestable [2], [3], [4]. Consequently, SGP holds significant promise as an alternative energy source.

The concept of SGP was first proposed by Pattle in 1954 [5] and has since expanded into a variety of methods by which to harness this chemical potential of mixing. The three primary means of producing salinity gradient power that have received the most attention are capacitive mixing, pressure-retarded osmosis (PRO), and reverse electrodialysis (RED) [6]. However, while recent research has focused primarily on the use of SGP for large-scale commercial power plants [6]–[10], little research has concentrated on the applications of SGP with regards to energy harvesting for small systems, such as unmanned underwater vehicles (UUV) or remote sensing devices. For such applications, specific and volumetric power density take precedence over those factors on which previous research has focused, such as the power output per membrane area (a

metric of power per cost) or the levelized cost of electricity. This thesis explores the feasibility of using RED as an environmental energy harvester for remote sensing devices and unmanned underwater vehicles, with a specific focus on the Arctic Ocean.

1.1 Salinity Gradient Power

1.1.1 Gibbs Free Energy of Mixing

During the uncontrolled mixing of two solutions of dissimilar concentrations the Gibbs free energy of mixing, ΔG_{mix}, is released to the environment. This released chemical energy represents the maximum potential energy that can be harvested through an engineering process. The Gibbs free energy released per mole during the mixture of two solutions is given below:

$$-\Delta G_{mix} = R_{gas}T \left(\begin{array}{c} \left[\sum x_i \ln(\gamma_i x_i)\right]_M - \phi_A \left[\sum x_i \ln(\gamma_i x_i)\right]_A \\ -\phi_B \left[\sum x_i \ln(\gamma_i x_i)\right]_B \end{array} \right) \qquad (0.1)$$

where R_{gas} is the ideal gas constant, T is the temperature of the mixture, x_i is the mole fraction of component i, γ_i is the activity coefficient of component i which accounts for the non-ideal behavior of the solution, and ϕ is the ratio of moles in solution A or B to that of the final solution M [1].

In the specific case of fresh and salt water mixing, both of which have relatively low concentrations, the mole fraction x_w and activity coefficient y_w of water are close to unity, causing their respective terms to drop out. Additionally, the concentrations of all other solutes are neglected, while the contributions of NaCl to the total volume and number of moles is minor. Then,

by assuming that the total volume of the mixing solutions is constant, one can approximate the mole fraction with the molar salt concentration as seen in equation ((1.2):

$$-\frac{\Delta G_{mix,V_A}}{\upsilon R_{gas}T} \approx \frac{c_M}{\phi_A}\ln\gamma_{s,M}c_M - c_A\ln\gamma_{s,A}c_A - \frac{(1-\phi_A)}{\phi_A}c_B\ln\gamma_{s,B}c_B \qquad (0.2)$$

where $\Delta G_{mix,V_A}$ is the Gibbs free energy per volume of solution A, υ is the number of ions into which each electrolyte molecule will dissociate into (2 for $NaCl$), and c is the molar concentration of $NaCl$ in solutions A, B, or M, and the subscript s denotes the activity coefficient specifically for salt [1].

Finally, one can assume ideal behavior such that the activity coefficients are negligible. Equation 1.2 can then be simplified to equation (1.3) [1]:

$$-\frac{\Delta G_{mix,V_A}}{\upsilon R_{gas}T} \approx \frac{c_M}{\phi_A}\ln c_M - c_A\ln c_A - \frac{(1-\phi_A)}{\phi_A}c_B\ln c_B \qquad (0.3)$$

1.1.2. Capacitive Mixing (CapMix)

Capacitive mixing was first proposed in 2009 [11] as an electrochemical means of directly producing electrical power, with RED previously being the only means of direct conversion. A capacitive mixing cell includes two electrodes, which are initially immersed in a high concentration salt solution and are connected via an electrical circuit. As shown in Figure 0-1, the process consists of four distinct parts:
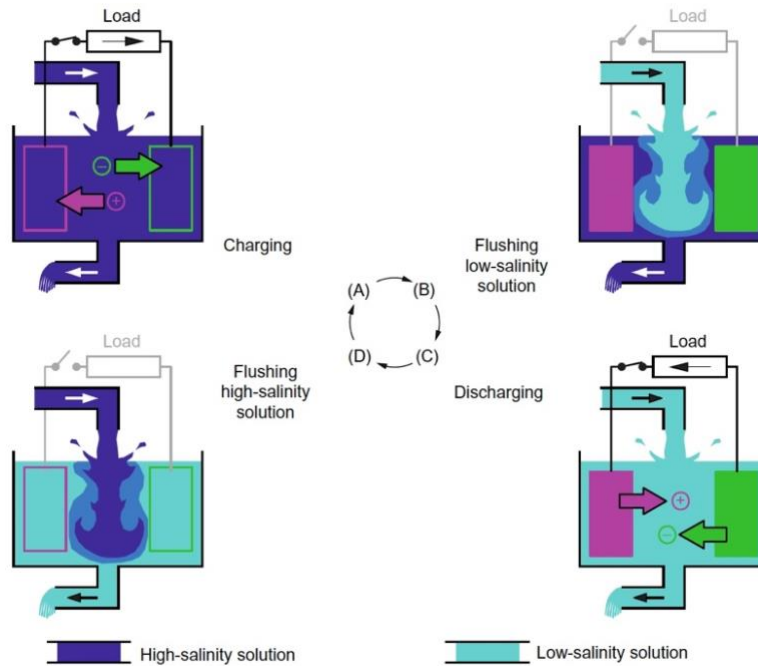
Figure 0-1: Four-step overview of the capacitive mixing cycle highlighting the system's conversion of chemical to electric potential

A. Current is applied to the electrodes, causing the electrodes to become charged. This induces cations (Na^+) and anions (Cl^-) to migrate to and form a thin layer on the negatively and positively charged electrodes respectively, in order to balance the local charges.

B. The circuit is disconnected and the high concentration solution is flushed with a low concentration solution. Replacing the high concentration solution with one of a lower ionic strength causes the thickness of the charged layer surrounding the electrodes to increase. This increases the electrical potential of the cell.

C. The circuit is reconnected. The lower concentration of the dilute solution induces some of the ions that have collected on the electrodes to discharge in order to approach chemical equilibrium, causing a charge imbalance on the electrodes. Consequently, the

charge collected on the electrodes flows through the circuit producing a current in the direction opposite to that applied in part A.

D. The circuit is opened and the low concentration solution is replaced with high concentration solution. Since the discharge of electrons in part C occurs at a higher electrical potential than when the current is applied in part A, net work is produced [7], [13].

While novel, capacitive mixing is still in the very early phases of its development and has not yet been put to use in real world applications. Its highest reported experimental power density of 0.2 W/m^2 is an order of magnitude smaller than those obtained for both PRO and RED [13]. Consequently, while it may hold future potential, capacitive mixing was not deemed a currently viable means of powering UUVs and remote sensing systems.

1.1.3 Pressure Retarded Osmosis (PRO)

The concept of PRO, first articulated by Sidney Loeb in 1975 [14], involves the production of mechanical power through the use of a water selective membrane to produce a pressure gradient. Figure 0-2 illustrates how PRO works. Two volumes of high concentration and low concentration fluids are separated by a semipermeable membrane that prevents the flow of ions from one solution to the other. Consequently, an osmotic pressure gradient is produced across the membrane, which drives water from the low concentration solution to the more concentrated solution. This increase in volume in the concentrated solution compartment can be directly harnessed to produce mechanical work or later converted to electrical work through a turbine.
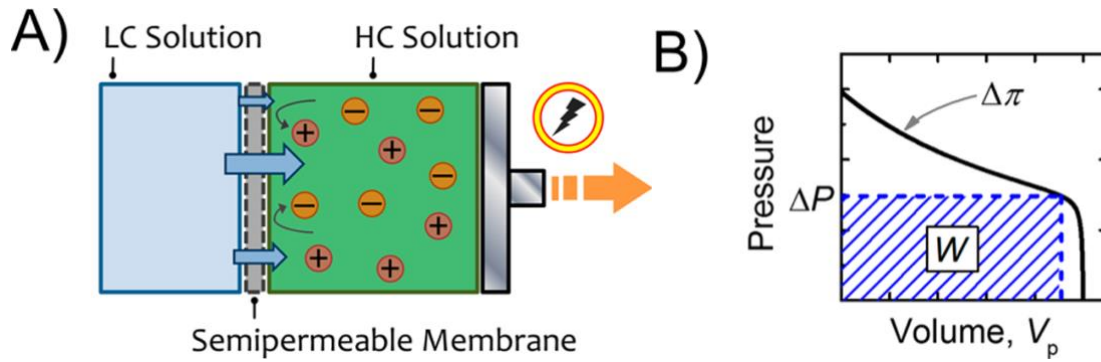
Figure 0-2: (A) Diagram illustrating the operation of PRO with water flowing across the semipermeable membrane from the low concentration solution to the high concentration solution and being harnessed to produce power. (B) Graph of the osmotic pressure $\Delta\pi$ versus the displaced water, V_p and the resultant useful work that can be achieved from a PRO system at a fixed applied pressure Δp [6].

The useful work that can be harnessed from PRO is found by integrating the applied hydraulic pressure, Δp, which in practical applications is constant, by the displaced volume of water, V_p, as given in equation (1.4) [6]:

$$W = \int \Delta p dV_p \qquad (0.4)$$

This useful work is depicted in Figure 0-2 (B) as the blue shaded region and is highly dependent on the selectivity and structural strength of the semipermeable membrane used [15]. A study by Yin Yip and Elimelech estimated the theoretical power density per membrane area and thermodynamic efficiency of PRO given the current technological state of PRO membranes to be between 2.4-3.7 W/m^2 and 44-54% respectively, depending on the concentration of the two mixing solutions [16].

PRO has seen a large growth in academic and commercial interest in the last ten years. Recent research has focused largely on improving membrane selectivity and structural strength, in addition to the application of PRO to areas with highly concentrated salt water, i.e. the Dead

Sea, and its use with reverse osmosis plants [15]. The power company Statkraft opened the first PRO power plant in Tofte, Norway in 2009, as can be seen in Figure 0-3, although plans for the plant's expansion were discontinued in 2014, due to the plant's low efficiency and uneconomical returns on investment [6].

Figure 0-3: Statkraft PRO Power plant in Tofte, Norway [17]

However, for the purpose of applying SGP to small unmanned vehicles or remote sensing devices, PRO was deemed a poor candidate. This decision was made because PRO would require a microturbine to provide electrical power, which generally has low efficiency. While PRO could be used as a direct propulsion system for UUVs, such a use would require a complete redesign of current long-range UUV platforms, which are largely powered electrically by lithium ion batteries [18].

1.1.4 Reverse Electrodialysis (RED)

RED was first proposed and demonstrated by Richard Pattle between 1954 and 1955 [5], [19] and saw further development with George Murphy's use of RED to power an electrodialysis (ED) desalination process, a process he named "osmionic demineralization" [20], [21]. Lacey further developed Murphy's concept in 1960 [22], but it was not until an impetus from the first and second oil crisis in 1973 and 1979 that interest in RED was truly heightened [23]. In 1976 Weinstein and Leitz improved the previous experimental power density achieved by Pattle by a factor of three to 170 mW/m^2 [24] and in 1980 Lacey published a paper modeling RED power production with varying parameters and the consequent costs associated with a commercial RED power plant [25]. In 2001 Veleriy Knyazhev reportedly conducted the first RED test in the field, using river and seawater [26]. In the following years extensive research has been carried out by the Wetsus Institute in the Netherlands on the topic, including five doctoral theses dedicated to the various aspects of RED [27]–[31]. Additionally, Bruce Logan from Pennsylvania State, Menachem Ehimelech from Yale, and Ngai Yin Yip from Columbia have published several articles analyzing the broader thermodynamic potential and constraints of RED and comparing it to other SGP systems such as PRO [1], [32]–[34].
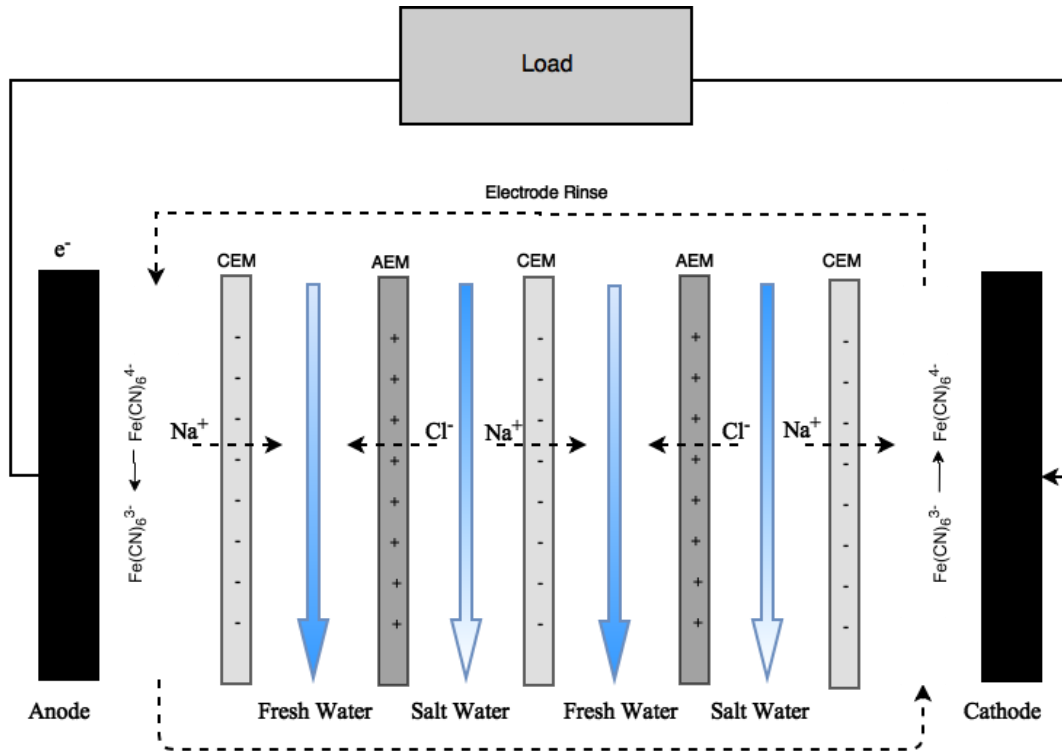
Figure 0-4: Schematic of an RED cell where a $K_4Fe(CN)_6$/ $K_3Fe(CN)_6$ solution is used as the electrolyte with inert electrodes

Figure 0-4 illustrates how an RED stack operates. High and low concentration water flow through alternating channels separated by a series of cation exchange membranes (CEM) and anion exchange membranes (AEM), which only allow the permeation of cations or anions respectively. As the water flows through the varying channels, ions from the high concentration solution will travel across the CEMs and AEMs due to osmosis to the less concentrated solution, creating an ion flux across the stack. In order to balance the charge at the respective electrodes, a redox reaction occurs and an electrical current is generated.

Analytically, the power generated by an RED stack is dependent on the total voltage across the stack, which is given in equation (1.5) as a derivation of the Nernst equation.

25

$$V_{stack} = n_{cell} \left(\frac{\alpha_{AEM}}{z_-} + \frac{\alpha_{CEM}}{z_+} \right) \frac{R_{gas}T}{F} \ln \left(\frac{C_H}{C_L} \right) \qquad (0.5)$$

For equation (1.5) n_{cell} is the number of cells, α is the permselectivity of the anion and cation exchange membranes, z is the ion valence (1 for Na^+ and Cl^-), F is Faraday's constant, and C is the concentration in g NaCl per kg of solution of the high (*H*) and low (*L*) concentration solutions respectively. Assuming that maximum power is achieved by matching the impedance, the power applied to the load is then:

$$P_{stack} = \frac{V_{stack}^2}{4R_{stack}} \qquad (0.6)$$

where R_{stack} is the stack's resistance.

Accounting for the pumping power the net power becomes

$$P_{net} = P_{stack} - P_{pump} \qquad (0.7)$$

The highest reported net power density per membrane area produced using fresh and seawater is 1.2 W/m^2 and was achieved by Vermaas in 2011[35], while the highest overall power density is 6.7 W/m^2, which Daniilidis et al. achieved in 2014 using fresh water and concentrated brine [36]. The characteristics of CEMs and AEMs have been the focus of much recent research with some studies exploring the effects of lowering membrane resistances through creating thinner stronger membranes [37]. Additionally, research has explored the possibility of using counter flow or cross flow (where the flows are 90° to one another), which have been shown to increase power output and efficiency, although once again stronger membranes would need to be developed to deal with the potential bending induced by dissimilar pressures along the channels [33]. New profiled membranes which omit the need for spacers, and consequently omit the spacer shadow effect (blockage of the membrane by the spacer), have also been shown to reduce the pressure drop

along the channel length, thus reducing pumping losses and greatly improving the overall net power [38]–[41]. The need to improve the monovalent permselectivity of CEMs and AEM has been identified as one area that could lead to significant improvements in the performance of RED, as the flux of even a few multivalent ions greatly reduces the power generated by 29% to 50% [42]. While RED research has focused heavily on membrane technology, the use of segmented electrodes along the length of the RED channel to better match the load and increase the maximum power output has also been proposed [43], [44].

Currently, two RED test power plants are in operation, one on the Afsluitdijk dam in the Netherlands and the other in Marsala, Italy. The RED plant in the Netherlands, pictured in Figure 0-5 was opened in 2014 with the aim of eventually producing between 0.5-2MW and is operated by REDstack, a spinoff from the Wetsus Institute in collaboration with Fujifilm. The plant utilized fresh water flowing from the Rhine and seawater from the Waddenzee to produce power, discharging the brine back into the sea to prevent the dam from flooding [45]. In contrast, the Reverse Electrodialysis Alternative Power (REAPower) Project in Sicily, sponsored by the European Union and REDstack, uses concentrated brine from a nearby salt works and brackish water. Research at the plant aims to achieve 1kW, with recent efforts achieving 700W using artificial saline solutions [9].

Figure 0-5: REDstack power plant situated on the Afsluitdijk dam between the Ijsselmeer and the Waddenzee [46]

In assessing RED's potential for use with small-scale mobile platforms, it is worth noting that while recent studies comparing RED and PRO have predicted a higher theoretical power density for PRO [16], RED has several unique advantages. These advantages include RED's ability to directly produce electrical power and a design that allows for more ready integration into current UUV and sensor systems, which rely on battery power. Consequently, RED was selected as the SGP technology best suited for potential future application into UUV and remote sensing systems.

1.2. RED Applications

1.2.1 Geographic Areas of Interest

As illustrated in equation (1.5) and equation (1.6), the power output from RED is proportional to the square of the logarithmic ratio of the high to low concentration. Consequently, the areas where RED can be applied are restricted to a limited number of key geographic regions. In addition to the river outlets typically envisioned for RED application, such as the Mississippi

River Delta, the Rhine River, the St. Lawrence River, etc., the polar regions also contain a

significant salinity gradient during the summer months.
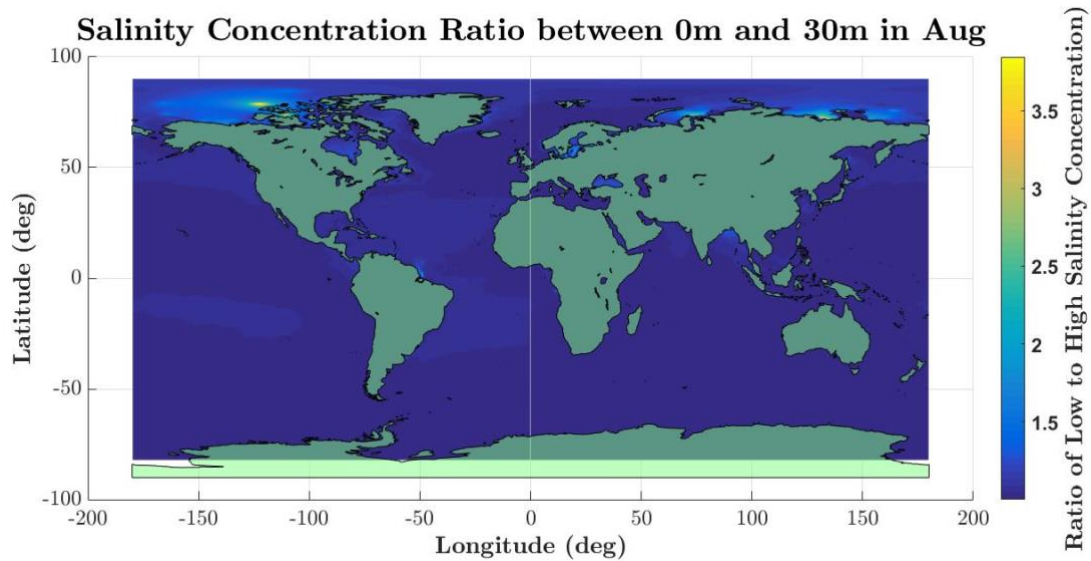
Figure 0-6: Global salinity ratio of the highest to lowest concentrations between 0 and 30m for
the month of August with data compiled from GDEM [47]

As shown in Figure 0-6, in addition to the mouths of large rivers, such as the Ganges and

Amazon, a substantial ratio of salt to fresh water can be found within the top 30 meters below

sea surface in the Arctic region. Additionally, it should be noted that the data in Figure 0-6 does

not accurately capture much of the local concentration gradient found in the Artic.

1.2.2 Application to the Arctic

The Arctic Circle has become a region of increased attention to both the scientific and defense

communities as of late. As the effects of global warming increasingly make their presence felt on

the world, the need to collect climate data for sustained periods in the Arctic region has grown in

importance. Additionally, from a security perspective, the melting of the icecaps will increase

demand for access to the region's new trade routes and abundant natural resources [48].

However, the region's harsh weather and currently significant ice-coverage, as depicted in Figure 0-7, continues to present a challenging operational environment. The predominant power sources in the region are diesel generators or batteries, both of which rely on costly periodic resupplies of fuel or, in the case of primary batteries, replacement.

Figure 0-7: Map of the Arctic Circle showing the minimum extent of sea ice both in 2012 (red line) and on average for the past 30 years [48]

As previously depicted in Figure 0-6, substantial salinity gradients develop in the Arctic during the summer months. Increased periods of exposure to sunlight cause small ponds of fresh water to form on the surface of the ice. Since the fresh water is denser than the ice, some of this water will percolate through the ice, forming small fresh water ponds on top of the denser seawater as depicted in Figure 0-8.
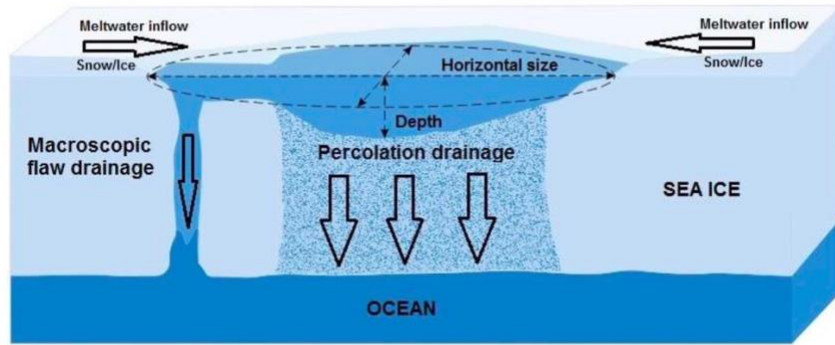
Figure 0-8: Illustration of how melt ponds on the surface percolate through the ice to create a boundary layer of fresh water [49]

These ponds lead to thin boundary layers directly below the ice with extremely sharp salinity gradients ideal for SGP. Protected from wind, these freshwater "ponds" persist for a sustained period of time, as shown inFigure 0-9, until a storm or other phenomena induces mixing. Through SGP, these sharp salinity gradients represent readily accessible energy reservoirs in an otherwise bleak and austere environment, barren of otherwise readily accessible power sources.
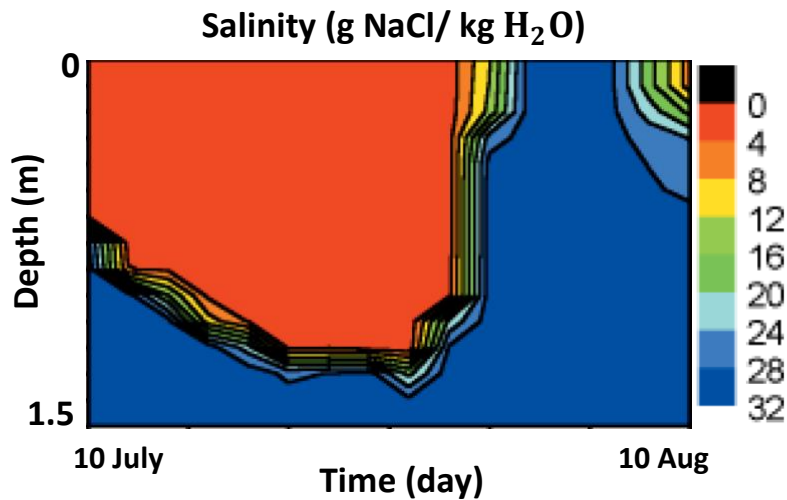
Figure 0-9: Salinity concentration directly under an ice floe between the months of July and August [50]

1.2.3 Applications to Small Mobile Platforms

As previously mentioned, RED holds potential for application to small UUV platforms or remote sensing devices facing certain environmental constraints. According to the U.S. Navy, lithium ion batteries are currently the power system of choice for small scale UUVs, due to their ability to be easily downscaled for platforms with volumetric limitations (in contrast to fuel cells or hybrid diesel/ rechargeable battery systems) and their high energy density in comparison to other battery systems [51]. However, lithium ion batteries are presently not sufficient to power a UUV for the breadth of the polar regions, where the smallest expanse covered by Arctic sea ice in recorded history is 1.3 million square miles [48]. While solar power has often been implemented to extend battery ranges in the past, photovoltaic power is not a viable option for travel under the ice or at significant underwater depths, with power outputs at depths of 8m falling to levels as low as 1.5% of that at the surface [52], [53]. Consequently, RED poses a potential means of energy harvesting to supplement traditional energy storage systems such as lithium ion batteries.

One potential means of travel for such a system would be a sinusoidal dive pattern, as depicted in **Error! Reference source not found.**, collecting fresh water at the surface and then travelling downward to collect salt water at around 25-30m underwater. A UUV could also consistently float under one iceberg where the salinity gradient is significantly shallow, as in Figure 0-9, harvesting energy under the ice while costing the system little propulsive power.
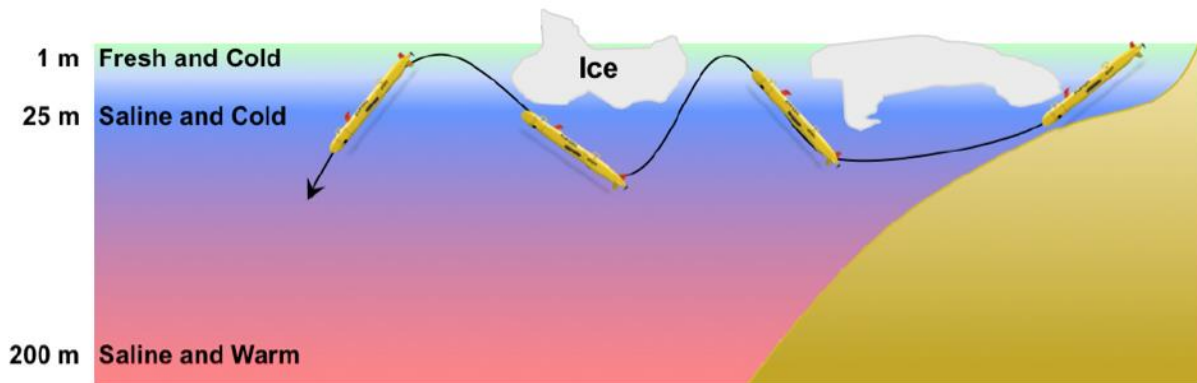
Figure 0-10: Proposed dive profile of a RED powered UUV

In addition to potentially supplementing existing UUV power systems, RED also holds potential for use with remote sensing devices. By tethering a remote sensing system under an iceberg, a sensor would be able to float around a region while harvesting power through RED, requiring only a means of vertical transport between the regions of differing concentration. RED could also be employed using the surface melt pond, depicted in Figure 0-8, as a fresh water reservoir and seawater for a high concentration source in order to produce power for a small sensing device on the surface. An application to river delta regions, where tidal currents allow for a predictable cycle of fresh and salt water, is the concept of tethering a buoy to the sea floor, which would collect fresh and salt water with the tides in order to produce power. Such a device could discretely collect data without any moving parts for an extended period of time, without having to rely on battery life and at a constant depth unobtainable for photovoltaic powered devices.

THIS PAGE INTENTIONALLY LEFT BLANK

Chapter 2
Computational Modeling

In order to form an analytical assessment of RED and its potential as a power source for remotely operated vehicles and sensing devices, a computational code modeling the underlying phenomena of RED was created from a combination of fundamental theoretical and empirical equations. The code was modeled on a similar approach taken by Vermaas [54], with additional adjustments made to focus on various aspects of RED pertaining to potential use by naval vessels. The model consisted of a parameter sweep of the key variables affecting a RED stack, i.e. the height h and length l of the active membrane area, the width between the membranes w, and flow velocity v, which are depicted in Figure 0-1. This parameter sweep then found the optimal dimensions and flow rates for a theoretical RED stack in order to maximize the net power density of the system at the optimal naturally occurring concentrations.

While past studies have either limited their models to specific RED stack designs with ample empirical validation or focused on broad assessments with limited experimental validation, this model assesses a wide range of possible RED stack parameters, while generating results largely consistent with a diverse range of past experimental studies. Unlike past studies, it focuses on optimizing the net volumetric power density, rather than the net power density per membrane area, as the volumetric power density is of greater concern for utilization in small mobile platforms. Additionally, the model accounts for the buoyant energy losses incurred by having to transport volumes of water of dissimilar densities from a specified depth to the surface and vice versa. Past studies had no need to account for these losses given RED's intended use for

commercial power. The model also incorporates the flexibility to estimate the net power

densities for both spacer-filled channels and those with profiled membranes, while providing

empirical validation for both designs. Finally, it considers the viscosity and density of water as

variables of the input temperature, pressure, and water concentrations, allowing for more

accurate power predictions in a diverse set of environmental conditions. These features allow for

an initially broad optimization of RED's design parameters followed by a more precise analysis

of its potential in the Artic versus other potential environmental energy harvesters.

2.1 Governing Equations and Assumptions

2.1.1 Key Assumptions

In constructing the computational model, several key assumptions were made in order to

simplify the modeling. These assumptions include:

1. Matched impedance between the stack and load ($R_{load} = R_{stack}$)
2. Flow between the channels can be modeled as laminar flow between two infinite parallel plates
3. A linear salinity gradient from the surface to the depth of 30m
4. The effects of parasitic currents are negligible.
5. The effects of membrane fouling are negligible.

For electrical power systems, maximum power is often achieved by matching the

impedance of the stack and load. While Weiner et al. showed that this is not the case, due to the

drop in voltage along the RED channel, this assumption nevertheless provides a conservative

estimate as to the maximum achievable power [10]. The assumption that the flow can be

modeled as laminar between two infinite parallel plates was shown to be valid, as the low flow

rates and small hydraulic diameter of the channels led to low Reynolds numbers for the parameter space of interest. This was verified by calculating the percentage of computational data points for which the flow was laminar, with the results coming close to unity. Additionally, the channel height in a RED stack is often several orders of magnitude greater than the channel width, thus justifying the approach of modeling the membranes as infinite parallel plates. The third assumption was necessary, primarily to effectively model the buoyant force losses incurred by transporting volumes of water with dissimilar densities. Regarding the effect of parasitic currents, Veerman et al. showed that through careful stack design these losses in efficiency could be reduced from 25% to 5%, mitigating these losses even for large stacks [55]. While the effects of membrane fouling have been shown to decrease net power density by as much as 40% within one day of testing [56], methods such as reversing the fresh and concentrated water channels and the development of membranes with improved monovalent selection can reduce these losses [57], [58].

2.1.2 Fundamental Equations

Stemming from the Nernst equation, equation (1.5) gives the theoretical voltage that is produced from the ion flux across the stack (refer to Appendix A for a table of the key variables and their units).

$$V_{stack} = n_{cell} \left(\frac{\alpha_{AEM}}{z_-} + \frac{\alpha_{CEM}}{z_+} \right) \frac{R_{gas} T}{F} \ln \left(\frac{C_H}{C_L} \right) \tag{1.5}$$

The power applied to the load is then

$$P_{stack} = I_{stack}{}^2 R_{load} \tag{0.1a}$$

$$P_{stack} = \frac{V_{stack}{}^2 R_{load}}{(R_{stack} + R_{load})^2} \tag{2.1b}$$

37

$$P_{stack} = \frac{V_{stack}{}^2 R_{load}}{[n_{cell} \times (R_{ohmic} + R_{Bl} + R_{\Delta C}) + R_{load}]^2} \tag{2.1c}$$

where I_{stack} is the current and R is the resistance due to the load, ohmic losses, boundary layer losses, and losses along the channel's length due to a decrease in the difference of concentration between the flows [54]. These resistances are dependent on various membrane and spacer properties, solution concentrations, and the specific dimensions of the stack itself as pictured in Figure 0-1.
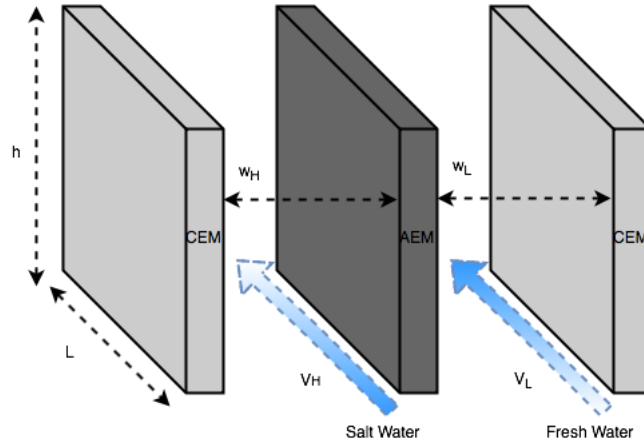
Figure 0-1: Schematic of the membrane orientation in a RED stack highlighting the key parameters which impact the stack's performance and were the subsequent focus of the computational modeling

The ohmic area resistance r_{ohmic} is due to electrical resistance from the membranes and the channels themselves as given below.

$$r_{ohmic} = \frac{1}{1-\beta} \cdot (r_{CEM} + r_{AEM}) + \frac{1}{\varepsilon^2 \cdot \frac{k_0}{C_0}} \cdot \left(\frac{w_H}{C_H} + \frac{w_L}{C_L}\right) \tag{0.2}$$

β is the masking factor due to the spacer shadow effect on the membrane, r is the area resistance of the CEM and AEM respectively, w is the intermembrane width of the high and low concentration channels, ε is the porosity of the channel between the membranes, k_0 is the electrical conductivity of seawater at standard temperature and pressure, and C_0 is the reference concentration of seawater (35 g NaCl per kg).

The boundary layer resistance due to concentration polarization across the membrane is given empirically by Vermaas et al. for both spacer-filled channels and profiled membranes [54].

$$r_{BL,spacers} = \left(0.62 \cdot t_{res} \cdot \frac{w}{L} + 0.05 \right) \tag{0.3a}$$

$$r_{BL,profiled} = \left(0.96 \cdot t_{res} \cdot \frac{w}{L} + 0.35 \right) \tag{2.3b}$$

with t_{res} as the residence time, which is the quotient of flow velocity v and the membrane length L. The resistance due to a decrease in concentration along the membrane length L can be approximated by (2.4a):

$$r_{\Delta C} = \left(\frac{\alpha_{AEM} + \alpha_{CEM}}{2} \right) \frac{R_{gas} \cdot T}{z \cdot F \cdot j} \ln \left(\frac{A_L}{A_H} \right) \tag{0.4a}$$

Where

$$A_L = 1 + \frac{j \cdot t_{res}}{F \cdot \varepsilon \cdot w_L \cdot \frac{C_L}{M_S}} \tag{2.4b}$$

$$A_H = 1 - \frac{j \cdot t_{res}}{F \cdot \varepsilon \cdot w_H \cdot \frac{C_H}{M_S}} \tag{2.4c}$$

With M being the molecular weight of NaCl and where j, the current density is given by:

$$j = \frac{V_{total}}{r_{stack} + r_{load}} \tag{0.5}$$

The derivation of equations (2.4a)-c) is given by Vermaas et al. [35]. Assuming a matched impedance equation, (2.1b) then becomes equation (1.5)

The pressure drop Δp along one channel was estimated using the Darcy-Weisbach equation for laminar flow between two infinite parallel plates as shown in equation (2.6) [59],

$$\Delta p = f \, \frac{L}{d_H} \, \frac{\rho v^2}{2} = \frac{48\mu L v}{d_H^{\,2}} \tag{0.6}$$

where d_H is the hydraulic diameter. In order to better account for the effect of spacers and profiled ridges in accurately predicting the pressure drop, the hydraulic diameters were adjusted [54]. The hydraulic diameter for spacer filled membranes is given by equation (2.7a) [60], while that of profiled membranes is given by equation (2.7b) [60], [61]:

$$d_h = \frac{4\varepsilon}{2/w + (1 - \varepsilon) \cdot S_{vsp}} \tag{0.7a}$$

$$d_h = \frac{4b \cdot w}{2b + 2w} \tag{2.7b}$$

where S_{vsp} is the ratio of the spacer surface area to its volume and b is the width between the profiled ridges (which was assumed to be proportional w). Using data from Vermaas et al. [35] for spacer filled channels, a fit equation as a function of intermembrane width was generated in order to calculate a correction factor K_p for the pressure drop for intermembrane distances between 60 and 485 μm, which is the parameter space of interest for optimization. This was accomplished by fitting the pressure drops at intermembrane distances of 61, 101, and 209, and 455 μm. As for profiled membranes, a correction factor was calculated using data provided by Güler et al. [39]. Further information regarding these correction factors can be found in Appendix B. The pumping loss for the entire stack is then:

$$P_{pump} = 2 \cdot n_{cell} \cdot Q \cdot K_p \cdot \Delta p \tag{0.8}$$

Where the volumetric flow rate is given by:

$$Q = \varepsilon \cdot h \cdot w \cdot v \tag{0.9}$$

Optimizing P_{net} from equation (1.7) as a function of the fluid velocity v, channel width w, channel height h, and channel length L (as depicted in Figure 0-1) given certain constraints, then allows one to approximate the idealized dimensions in order to achieve maximum net power per volume stack.

In addition to conducting a parameter sweep in order to predict the potential net power of a RED stack given certain design specifications, estimates unique to the use of RED for a UUV were also considered. The most prominent of these additional considerations was the power losses due to overcoming the buoyant force acting on solutions of differing densities. This buoyant force loss occurs due to the need to transport denser high concentration seawater through less dense water to the surface and similarly from transporting less dense freshwater to lower depths through denser seawater.

Assuming a linear salinity profile the energy E required to transport a volume of water V was estimated using equation (2.10) below,

$$\frac{E}{V} = \frac{1}{2}\left(\rho_{top} - \rho_{bot}\right) \cdot g \cdot y \tag{0.11}$$

where ρ is the density of water at the top and bottom of the UUVs dive profile, g is the acceleration due to gravity, and y is the vertical distance traversed by the UUV from the top to the bottom of its dive cycle. This is then used to calculate the consequent loss in power, $P_{buoyant}$ in equation (2.11):

$$P_{buoyant} = 0.75 n_{cell} \cdot \frac{E}{V} \cdot Q$$

$$\tag{0.10}$$

Accounting for $P_{buoyant}$ one can find the actual power available to provide thrust or power for electronic instrumentation for a UUV or sensor system as shown in equation (2.12) below.

$$P_{net,mod} = P_{stack} - P_{pump} - P_{buoyant} \qquad (0.12)$$

The thermodynamic properties of water including its density, dynamic and kinematic viscosity used in the model were obtained via Matlab scripts produced by Sharqawy et al. [62] and Nayar et al. [63], given inputs of temperature, pressure, and salinity concentration.

2.2 Model Implementation

The computational model was run on MATLAB utilizing a 4D matrix, which contained the four variables of interest regarding the design and operation of a RED stack. These values were then used to compute matrices for the stack's voltage, ohmic resistance, boundary layer resistance, and resistance due to the concentration drop along the channel with each point within the matrix corresponding to a unique combination of variables. A Levenberg-Marquardt solver was then used to solve for the current density j produced by solving equation (2.13)

$$0 = j - \frac{V_{stack}}{2n_{cell} \times (R_{ohmic} + R_{Bl} + R_{\Delta C}) + R_{elec} + R_{CEM}} \qquad (0.13)$$

and its subsequent Jacobian. Using these values, the gross power generated by the RED stack, P_{stack}, was computed. Subsequently the pumping losses were calculated and subtracted from the gross power to find the net power, P_{net}.

The model was initially run varying the intermembrane width w, channel length L, flow velocity v, and channel height h. Membrane properties for a profiled AEM from Güler et al. [39]

42

were primarily used for both CEM and AEM membrane properties, as these were deemed to be the state of the art and yielded higher power densities in agreement with the simulation performed by Vermaas et al. [54] and the experimental testing performed by Güler et al. [39]. Later iterations focused solely on varying the channel widths and flow velocities of the respective low and high concentration solution channels.

2.3 Model Validation

2.3.1 Validation for Spacer-Filled Channels

In order to validate the model, experimental results from Vermaas et al. [35] and Veerman et al. were compared to the model for the spacer-filled case, while results from Güler et al. [39] were used for the profiled membrane case. For both the spacer-filled channels and the profiled channels, comparisons were made between the area resistances, gross power densities, the pressure drops, and the net power densities.

Since the study by Vermaas et al. included measurements at intermembrane distances of 61, 101, 209, and 455µm, the spacer-filled model was consequently evaluated at several channel widths, allowing a more complete validation in the wider parameter space. This section limits comparison to the total resistance, predicted and experimental gross power, and pressure drop for the 101 µm RED stack, as this was the width at which the highest power density was measured [35]. Further comparisons for the total resistances, gross power densities, pressure drops, and net power densities at all four intermembrane widths can be found in Appendix C.
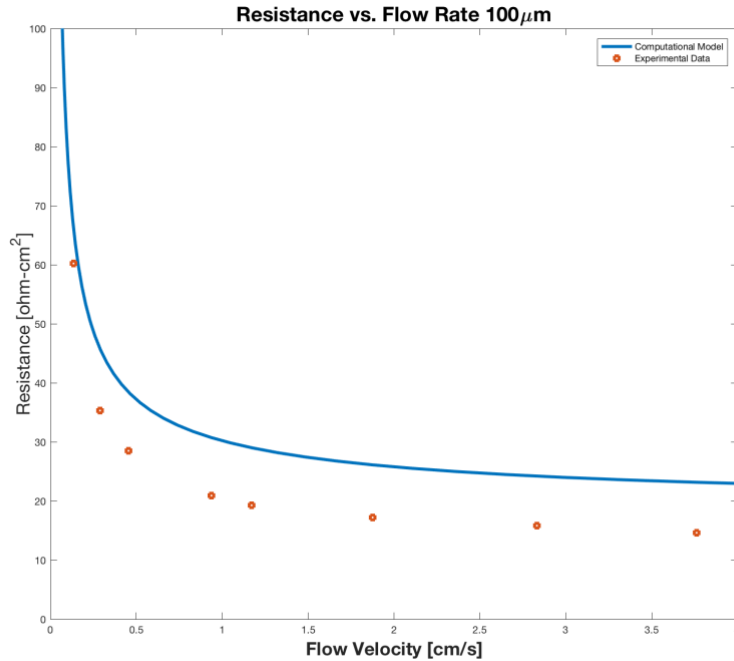
Figure 0-2: Comparison between the model and empirical results for the area resistance per cell produced by a five cell RED stack with nominal intermembrane widths of 100 μm [35]

Figure 0-2 shows that area resistance predicted by the model is consistently higher than that measured by Vermaas et al. As the resistance curve levels off beginning at a velocity of 1 cm/s, the model consistently differs from the experimental data by approximately $8.5 \, \Omega - cm^2$. Upon examining the individual components of the total resistance, it is found that the largest discrepancies occurs for the ohmic resistance and the boundary layer resistance. The error for the boundary layer equation most likely stems from the natural limitations of the empirical model given by Equation (2.3a), which was derived from a linear fit ($R^2 = 0.72$) [54]. The largest source of differences in ohmic resistance stems from discrepancies in the resistance produced by the spacer, which likely is due to the challenges in accurately modeling the effects of ε on the channel resistance, with its effect in equation (2.2) merely given as a first approximation [61].
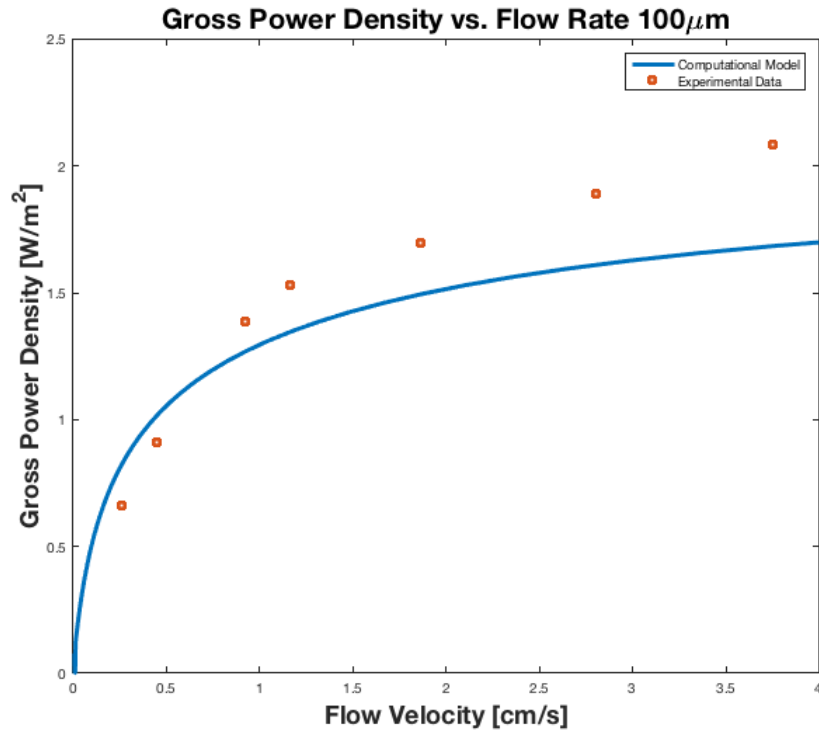
Figure 0-3: Comparison between the model and empirical results for the gross power per membrane area produced by a five cell RED stack with nominal intermembrane widths of 100 μm [35]

Figure 0-3 depicts the theoretical prediction of the gross power produced compared to the experimental values measured by Vermaas et al. It can be seen that the experimental results appear to lag behind the model by several tenths of a cm/s, while the model predicts power outputs consistently lower than those measured once the curve's slope begins to level off at around 1 cm/s. This can be traced back to a comparison in total resistances, as depicted in Figure 0-2, where Vermaas reported resistances consistently lower than those estimated by the model. While the difference between resistances remains relatively constant, at higher voltages and lower resistances the difference between the theoretical and experimental gross power densities

becomes more pronounced. However, slightly lower power outputs were expected, since the load was matched to the stack resistance, which has been shown to be suboptimal [10].

Figure 0-4: Comparison between the model and empirical results for the pressure drop across the length of a single channel in a five cell RED stack with nominal intermembrane widths of 100 μm [35]

Figure 0-4 shows close alignment between the pressure drops, as expected given that the pressure drop was fit to the empirical data. The only variation of note occurs due to that the best fit line was fixed to the origin, while the trend line for the experimental data was slightly offset.

An additional comparison was also made between results collected by Veerman et al. [64] with a 50 cell stack with intermembrane distances of 200 μm. This was done primarily to check the validity of the model with regards to the pressure drop for other stacks. The maximum error was found to be 22% in comparing the root mean square difference and the largest

measured pressure drop by Veerman et al. A summary of the root mean square errors between the various empirical data sets can be found in Table 0.1.

2.3.2 Validation for Profiled Membranes

For the profiled membrane case, the model was compared to a study in which a RED stack with microstructured AEMs with geometrical structures of pillars, waves, and ridges were compared to a stack with standard flat AEMs and spacers. The CEMs for all four scenarios, however, were flat and employed traditional net spacers. Comparisons were made to the pillared case, as these were reported as having produced the highest net power [39]. Greater variation between the computational model and experimental values were found in the case of profiled membranes. This is partially because profiled membranes are a novel development and thus not as well characterized analytically as their spacer-utilizing predecessors.
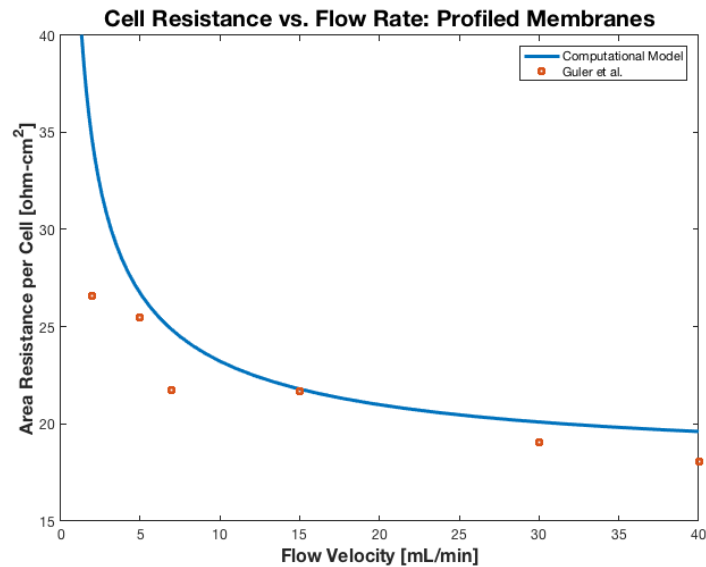
Figure 0-5: Comparison between the model and the empirical results for the total ohmic area resistance per cell in a two cell RED stack with pillar profiled AEMs [39]

In comparing the total resistance of the model with that measured by Güler et al., as done in Figure 0-5, it can be seen that while the resistances match fairly well, there is a significant discrepancy between the first data point and the model. This can be attributed to the fact that while the model holds constant the ohmic resistance contributed by the membranes and water compartments, these resistances are in fact slightly smaller at low flow rates before later approaching a steady state value [35], [39]. This is due to the fact that at higher flow rates the concentration of the dilute solution changes little along the channel length, increasing its resistance and consequently r_{ohmic} [35]. This initially lower ohmic resistance partially offsets the high resistance provided by the large concentration drop along the channel, resulting in a lower total resistance as reported by Güler et al. than that predicted by the model.
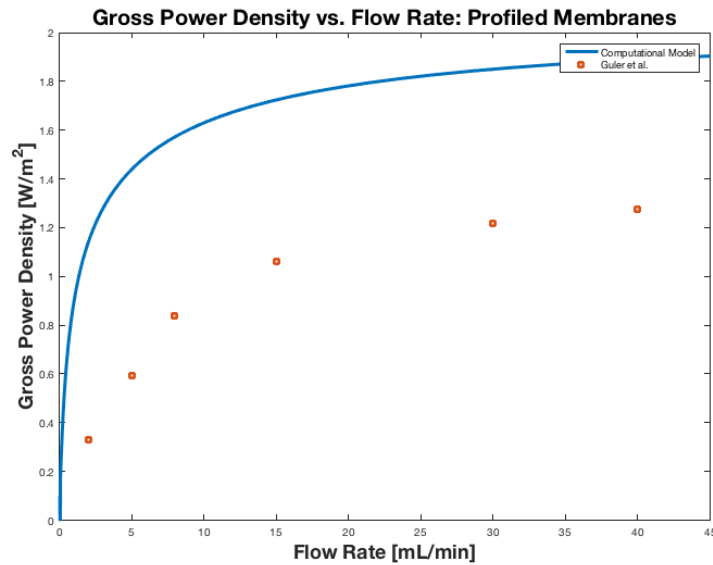
Figure 0-6: Comparison between the predicted and measured gross power density for a RED stack with pillar profiled AEMs [39]

Figure 0-6 shows a substantial increase in the theoretically predicted gross power density when compared to the experimental values, with a difference of 0.44 W/m^2 between the

maximum measured value and its corresponding point on the curve. A smaller offset in the x-axis similar to that seen in Figure 0-3 can also be observed. Given the relatively close correspondence between the measured and predicted resistances, the discrepancy must come from the voltage generated across the stack. Sources of discrepancy here may result from error in the reported permselectivities of the membranes as given by Güler et al. or the possibility of other unaccounted losses that occurred during experimental testing such as parasitic currents. The first three data points depict large discrepancies with the predicted values, but these were reported by Güler et al. to have a large uncertainty of up to 0.2 W/m^2 [39]. The last two data points at flow rates of 30 and 40 ml/min, had lower uncertainties and a consistent offset from the model, suggesting that the true offset between the empirical and computational results to be approximately 0.45 W/m^2. Nevertheless, both the theoretical and empirical values follow trends consistent with one another, indicating an error not rooted in the behavior of the fundamental governing equations.
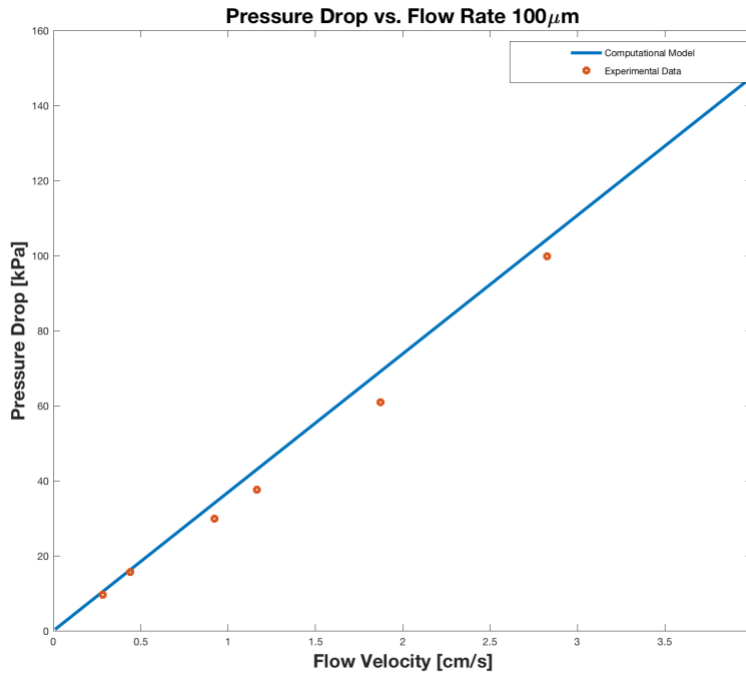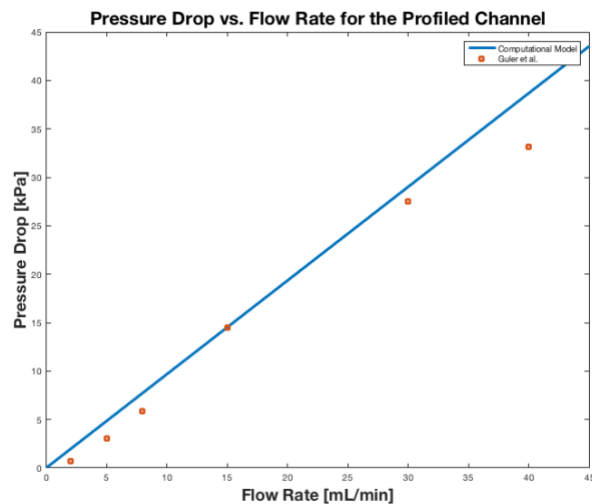

Figure 0-7: Comparison between the model and empirical results for the pressure drop across the length of a single profiled channel in a two cell RED stack with nominal intermembrane widths of 100 μm [39]

Similar to the case of the spacer filled channels, the pumping losses for the profiled

membranes were fitted to the empirical values reported as seen in Figure 0-7. Consequently, the

greatest discrepancy between the computational model and the empirical values is the offset

caused by setting the model's intercept at the origin. Additionally, it is worthwhile to note the

substantially lower pressure drop, which occurs across the channel length for profiled

membranes, in comparison to the spacer-filled channel in Figure 0-4. Further comparisons

between the total resistance, the net power, and different intermembrane distances can be found

in Appendix C.

Table 0.1: Root Mean Square Deviations of the Model Compared to Experimental Data

	Total Resistance $(\Omega - cm^2)$	Gross Power Density (W/m^2)	Pressure Drop (kPa)	Net Power Density (W/m^2)
Spacer- 61 μm [35]	5.52	0.257	46.14	0.316
Spacer- 101 μm [35]	8.49	0.239	5.12	0.156
Spacer- 200 μm [64]		.0865	2.115	0.124
Spacer- 209 μm [35]	17.13	0.1581	0.919	0.105
Spacer- 455 μm [35]	17.78	0.0868	1.377	0.0833
Profiled [39]	5.77	0.586	4.33	0.600

A summary of the root mean squared deviations of the model in comparison to the

experimental values for all four of the various intermembrane distances, as well as for the

profiled membrane, can be found in Table 0.1. It is critical to note that slight offsets in the x-axis

(in this case flow velocity or flow rate) can lead to substantial RMSDs given the slope is

substantially steep, as was the case at low flow rates. At times, this led to seemingly large

variations in the net power, as can be observed in Appendix C, when the actual variation in the

curves themselves was much smaller.

THIS PAGE INTENTIONALLY LEFT BLANK

Chapter 3

Computational Results

Implementing the model previously described, approximations were made as to the optimal design configurations for a RED stack in order to maximize the net volumetric power density. This configuration was then used to estimate the modified net volumetric power density of a RED stack at various fresh and salt water concentrations within environmental conditions specific to the Artic. RED was then compared to other environmental energy harvesting systems on a per mass and volume basis. Finally, the time required for a RED stack to recharge an equal volume and mass of lithium ion battery was calculated in addition to the length of time at which a RED unit would be able to provide greater power than a lithium ion battery of equal mass or volume.

3.1 RED Stack Design Optimization

Fixing the temperature at 298 K and the low and high concentrations at 1 and 30 g NaCl/ kg H_2O respectively, an initial parameter sweep was run. Figure 0-1 depicts the optimal design space for RED with regards to generating the most power per RED stack volume. The figure shows the variations in the net power density produced by a RED stack while fixing two design parameters at their optimums (as determined by the values which generate the greatest volumetric power density) and varying the other two parameters.
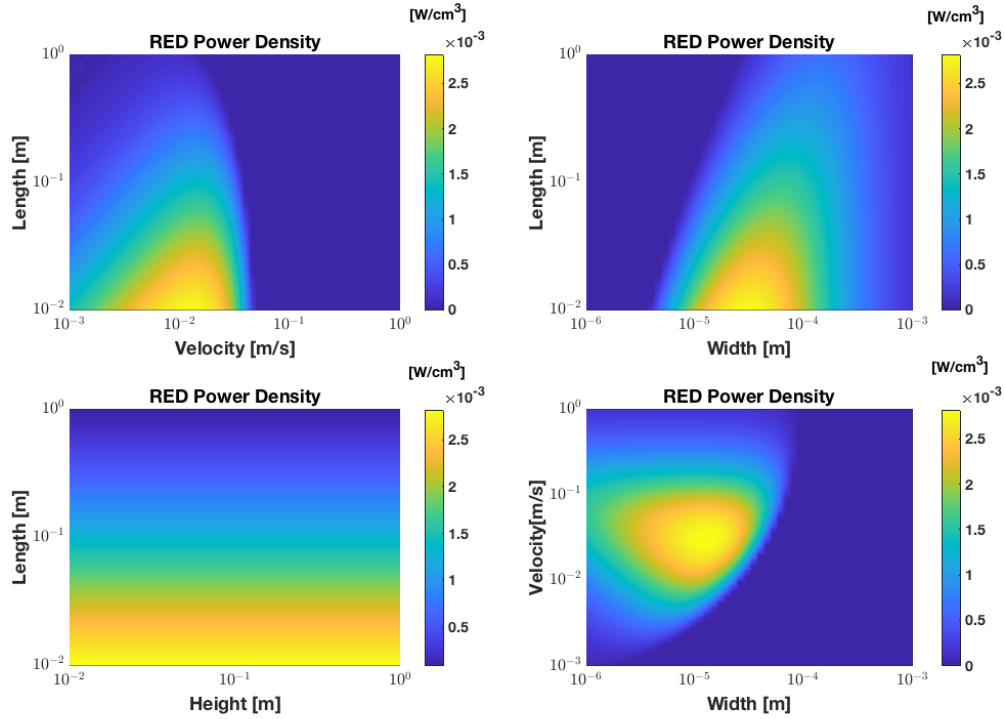
Figure 0-1: Net power per RED stack volume as a function of two RED stack design parameters using profiled membrane characteristics from Güler et al. [39]

The contour plot in the top left corner of Figure 0-1 depicts the power density as a function of the length and flow velocity, while maintaining the stack's height and intermembrane width constant. Figure 0-1 shows a precipitous drop in power density for velocities greater than approximately 30 cm/s for almost all lengths, although at greater flow lengths the drop-off occurs at even lower velocities. This is caused by the pumping losses which increase exponentially with increasing flow rate, as seen in equations (2.6), (2.8), and (2.9). Additionally, the optimal power density is reached at the smallest length allowed by the parameter sweep.

The top right plot in Figure 0-1 compares the effects of length and width on the power density, depicting an image that almost appears to be a reflected duplicate of the comparison between length and velocity. This an indication of the similar dominating effects of pumping

54

losses. In this case the net power drops off precipitously for intermembrane widths less than

10μm, due to the pumping losses which are proportional to $\sim \frac{1}{w}$ for profiled membranes

(assuming that the distance between profiled ridges is directly proportional to the intermembrane

width as done here). A more gradual decrese in net power density is observed with increasing

widths and increasing channel length. Once again the optimal power density appears to have no

bounded optimum with regards to length.

The bottom left plot in Figure 0-1, shows the invariant nature of the volumetric net power

density as a function of height. The power density is constant with regards to stack height, while

it gradually decreases with increasing channel length. The final bottom right figure illustrates

how power density is related to both velocity and intermembrane width, depicting an absolute

maximum of over 0.0025 W/cm^3 at a channel width of approximately 110 μm and a flow rate of

3 cm/s. This indicates that the both channel width and velocity can be optimized for maximizing

the power per volume RED stack.

When using the model to optimize for net power density per membrane area, the

predicted parameters were found to align relatively well with the theoretical results for profiled

membranes computed by Vermaas et al. They predicted maximum net power densities at

velocities of 4.2 cm/s and widths of 52 μm, whereas the model found optimal values at 2.6 cm/s

60 μm at a fixed height and length of 10 cm [52]. These variations likely stem from differences

in calculating the pumping losses.

Power Density vs. Width at Optimal Conditions

Power Density vs. Velocity at Optimal Conditions

Power Density vs. Height at Optimal Conditions

Power Density vs. Length at Optimal Conditions
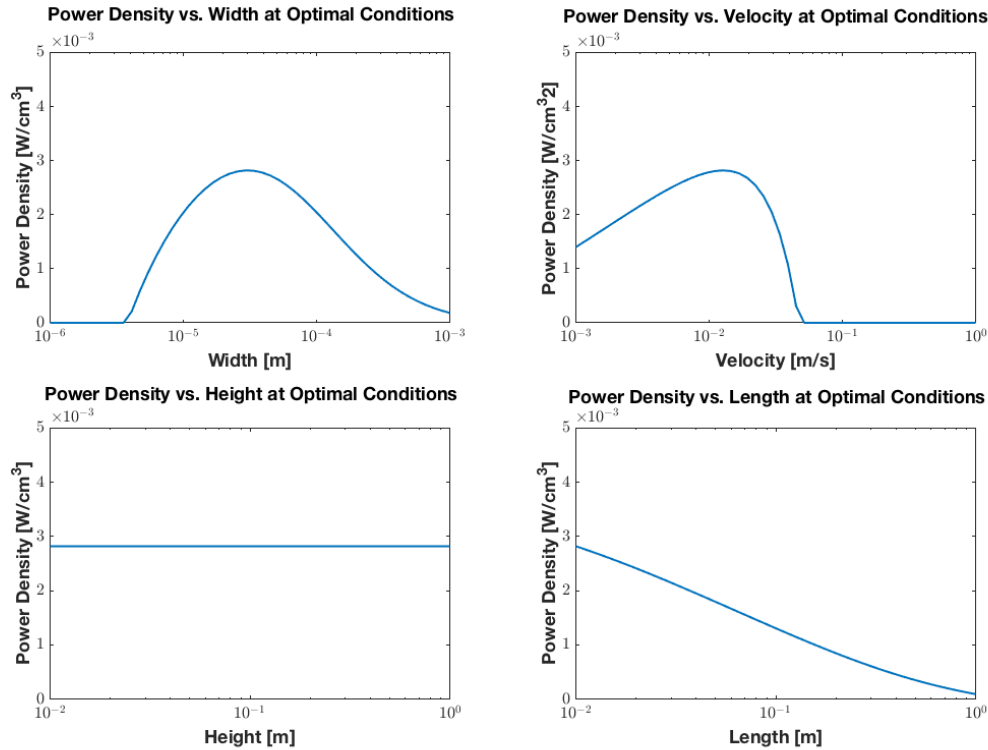
Figure 0-2: Design optimization curves for a RED stack with profiled membranes which show the maximum power density achievable while holding all other variables constant at previously determined optimums

In order to more easily look at the effects of varying solely one variable, Figure 0-2 depicts four plots of the volumetric power density versus one independent variable, while holding the others at their designated optimums. First, as suggested by Figure 0-1, the bottom left hand plot shows that the net power density does not vary as a function of membrane height. This is because, while the overall cell volume increases, the height of the cell does not affect the transport properties considered in equations (2.3a)-(2.4a) nor the pressure drop accounted for in equation (2.6). Additionally, while the top two plots in Figure 0-2 show that the net power density has local optimums for both flow rate and intermembrane distance, it is unbounded with respect to the length L of the flow path, as shown by the bottom right figure. This prediction is in

56

agreement with previous literature and is due to the fact that the concentration gradient between solutions decreases along the channel length [44]. This decrease in concentration results in lower voltages along the channel length and thus less power per unit length and from the linear relationship between the drop in pressure and channel length, as shown in equation (2.6). Thus, tall membranes with short lengths are desirable for producing large amounts of power at high power densities. Such designs, however, face structural limitations in order to maintain membrane stability.
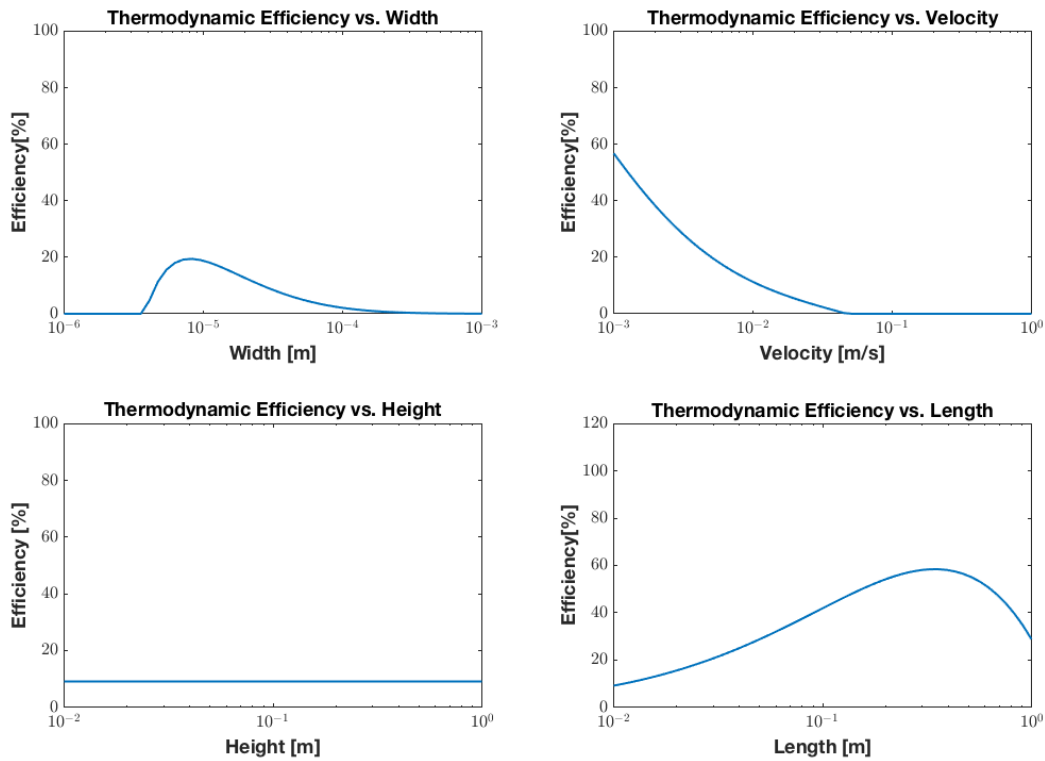
Figure 0-3: Optimization Curves depicting the thermodynamic efficiency of a RED Stack while holding all other variables at their designated optimum in order to achieve the highest volumetric power density

Figure 0-3 displays the thermodynamic efficiency of the RED stack versus one design parameter, while holding the other parameters constant at their designated optimums with regards to volumetric power density. This efficiency is found by comparing the net power to the ideal Gibbs free energy of mixing. A brief comparison of Figure 0-2 and Figure 0-3 shows that design parameters for achieving the maximum efficiency and power density differ. While the plot shows that the design optimum for width regards to efficiency is at smaller intermembrane distances than that for power density, changes in height are shown to have no affect in either case. The top right plot in Figure 0-3 shows that as velocity decreases the efficiency increases exponentially. This phenomenon is because as the flow rates are lowered, the pumping losses decrease and the solutions are allowed to approach chemical equilibrium, allowing more energy to be harvested, but resulting in much lower power. The bottom right plot depicts how efficiency increases with length up to a certain optimum. As the length increases, the solutions are allowed more time to equilibriate and more energy is recovered. However, at a certain point, the losses from pumping the solution over a longer length overtake the gains from a longer flow length.

Since Figure 0-1 and Figure 0-2 show that the volumetric power density was unaffected with respect to height and unbounded with regards to length, future optimization focuses on varying the widths of the low and high concentration channels as well as their flow rates, a design point previously noted by Veerman et al. [44]. A length of 10 cm and a height of 20 cm was selected for future RED optimization, as these dimensions maintain membrane structural stability while also minimizing flow length and maintaining sufficient membrane area for useful power production at a practical size for utilization within a UUV.
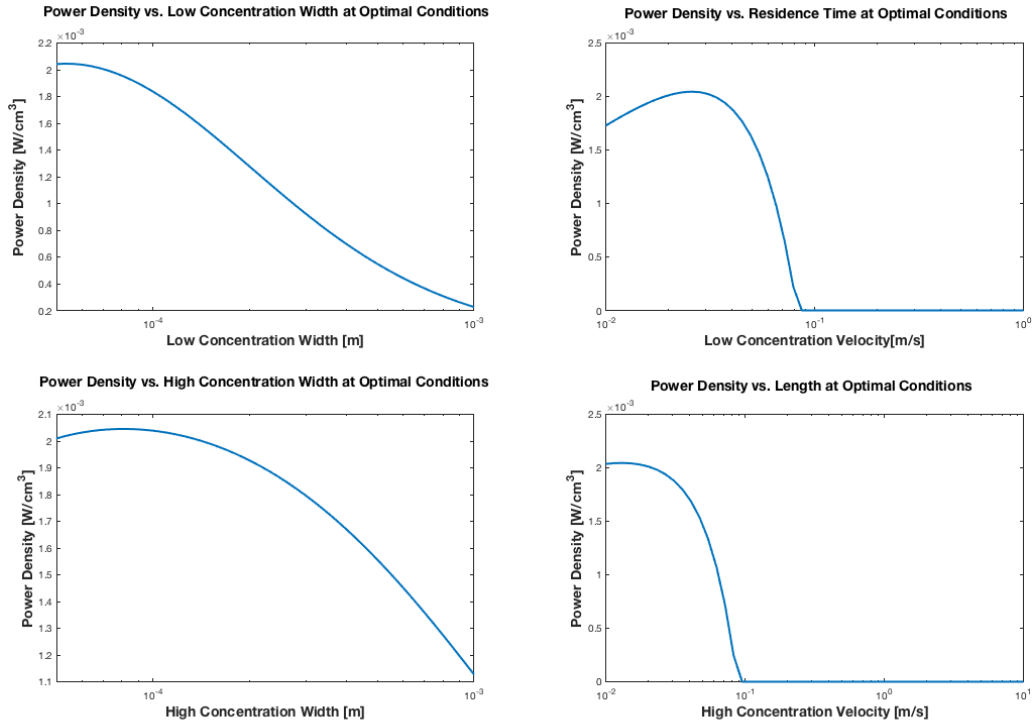
Figure 0-4: Design optimzation curves (using 50^4 data points) for a 50 cell RED stack using pillared profiled membreanes with a fixed flow length of 10 cm and height of 20 cm with varied high and low concentration channel widths and flow rates. The optimum channel width and flow velocity were found to be 53.2 μm and 81.5 μm and 3.91 cm/s and 7.54 cm/s for the low and high concentration channels respectively.

Figure 0-4 illustrates that for a 50 cell RED, stack differing optimums for the high and low concentration channel widths and flow channels exist. This is due to the varying concentrations in the two channels and the consequent differences in electrical conductivity between the channels. While smaller intermembrane distances reduce the electrical resistance of the solution, it also increases hydraulic lossses. Similarly, high flow rates reduce the boundary layer resistance due to increased mixing, and reduce the resistance created by the concentration drop along the channel by allowing less time for the diffusion of ions across the membranes (this comes at the expense of thermodynamic efficiency), but increase hydraulic losses [35]. As

Figure 0-4 clearly illustrates, the optimal channel width for the dilute channel is smaller than that of the concentrated channel, as the low conductivity of the channel has a more dominant effect on decreasing the power output than pumping losses in comparison to the more concentrated channel. With regards to flow velocity, the higher concentration channel is optimized at a faster flow rate than its low concentration counterpart in order to prevent a drop in concentration along the channel length, which would result in increased electrical resistance further along the length of the stack. Furthermore, for a matrix of 50^4 points, the model predicted that maximum power density per unit volume occurred at intermembrane distances and flow velocities of 53.2 μm and 81.5 μm and 3.91 cm/s and 7.54 cm/s for the dilute and concentrated channels respectively for an RED stack with a fixed length of 10 cm and height of 20 cm using pillared profiled membranes.

3.2 Predicted Performance Characteristics

Using these optimum channel widths and flow rates, the modified net power $P_{net,mod}$ per volume stack was estimated for varying salinity levels of both high and low concentration solutions at a temperature of 4°C. As shown in Figure 0-5, the maximum useful volumetric power density was found to be 1.55×10^{-3} W/cm^3 at concentration of 0.70 and 35 g NaCl/ kg H$_2$O. It is worthwhile to note that the maximum power density is not achieved with completely fresh water. Referring to equation (2.2), it can be seen that as the concentration of the fresh water C_L approaches zero, the resistance of that channel tends towards infinity. This effect occurs because the ions necessary for the transport of charge are being depleted. Thus, while a low concentration is crucial to achieving a high voltage, as seen in equation (1.5), and consequently

a high net power, it must be balanced with the electrical resistance of the low concentration channel.
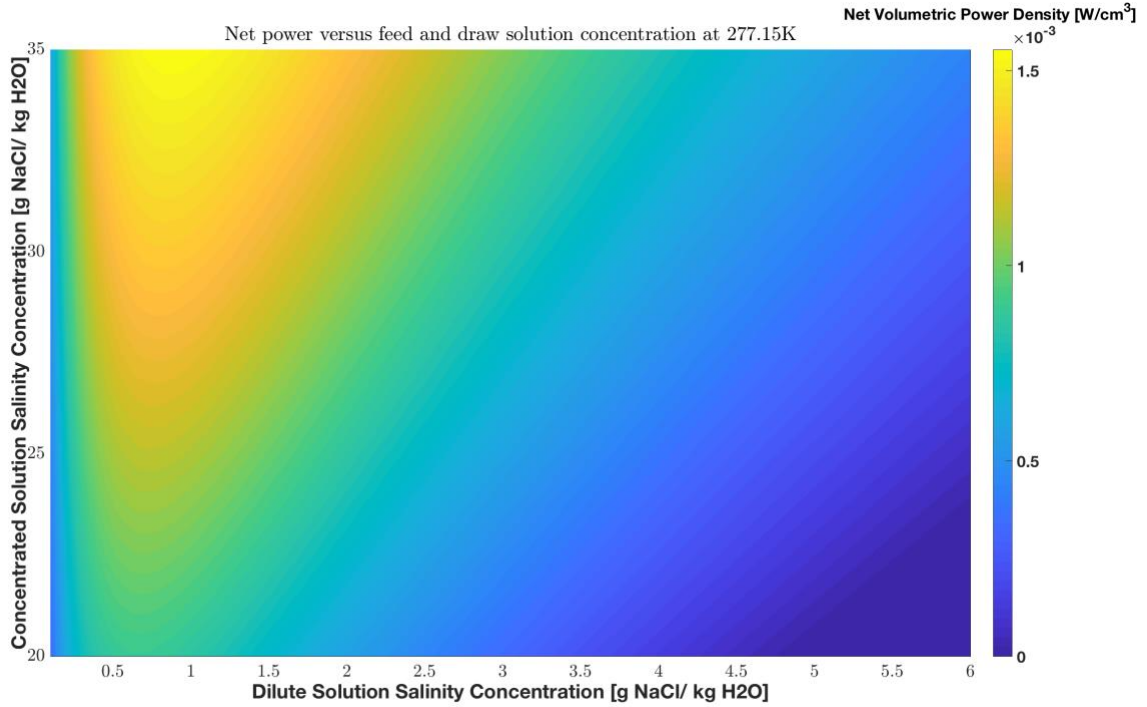
Figure 0-5: Net power production for a 100 cell RED stack operating around 4°C over a depth of 30m as a function of draw and feed solution concentration in practical salinity units

Finally, the model was used to gauge which variables have the greatest effect on the net volumetric power density produced by RED. This was assessed by varying a number of the key variables affecting the net power by +/- 5% from a series of baseline values as illustrated in Table 0.1. While this method presupposes a linear relationship between the variables and the modified net power production, which is not always the case, it nevertheless offers a helpful picture of those factors that affect the technology most potently.

Table 0.1: Baseline Values for Tornado Plot

Variable	Baseline Value
Temperature (K)	298
Membrane Permselectivity	0.90
Profiled Membrane Resistance ($\Omega - cm^2$)	100
Low Salinity Solution Concentration (g NaCl/ kg H_2O)	1
High Salinity Solution Concentration (g NaCl/ kg H_2O)	30
Length (cm)	10
Height (cm)	10
Low Concentration Width (μm)	100
High Concentration Width (μm)	100
Spacer Porosity	0.90

Figure 0-6 shows that temperature has the largest effect, as can be deduced from equations (1.5) and (1.6), since the temperature term T is squared in determining the power produced by the stack. Additionally, as shown in Appendix D, water's dynamic viscosity increases rapidly with decreasing temperature, leading to exponential increases in hydraulic losses, especially at low intermembrane distances. Following temperature, the membrane permselectivity α was shown to have the next greatest impact on the net power, as it is similarly squared in equation (1.5). The spacer porosity also had a large effect on the net power, as increasing its value reduces the ohmic and concentration drop resistance, as given by equations (2.2) and ((2.4a)-c). This is because highly porous spacers allow better flow of the solution along the channel, minimizing the concentration drop, and allow greater channel area for ion transport. Figure 0-6 then shows that variations in the high salinity solution concentration have a notable impact on the volumetric power density. This is because the net power is proportional to the squared log of the ratio of the concentrated to dilute solution concentration. Additionally, since the concentration of the salt water is more than an order of magnitude greater than that of the low concentration solution, a 5% variation has a much greater influence. The dilute channel width

and stack length also exert a meaningful influence on the net power output while the membrane resistance, dilute solution concentration, and the high concentration width were shown to have a much smaller relative effect on the power density as a whole.
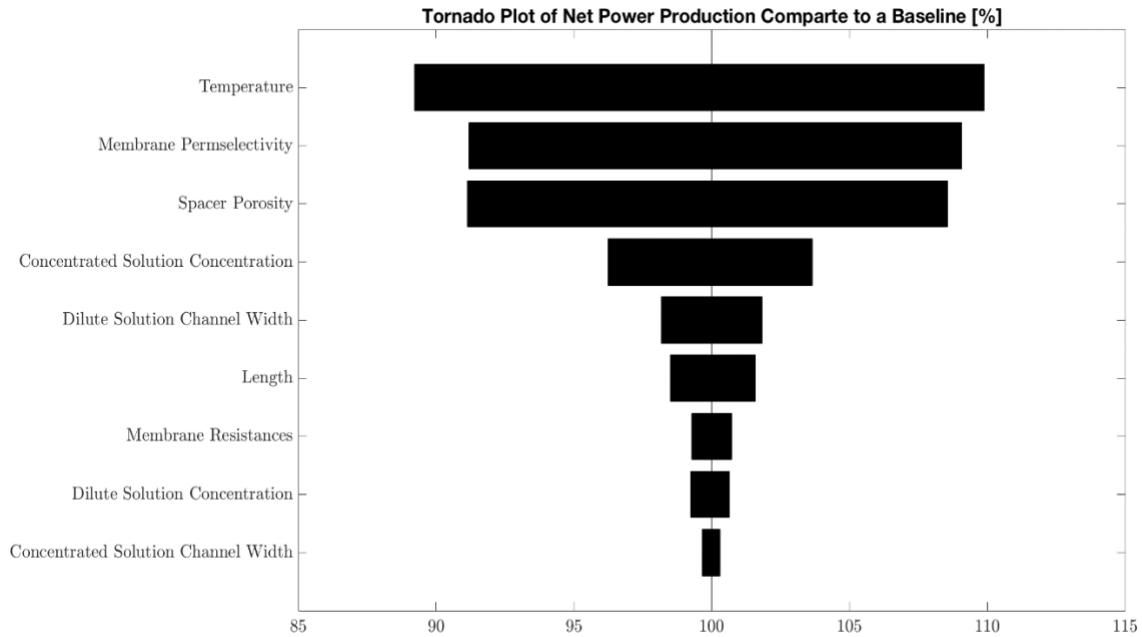
Figure 0-6: Tornado Plot of RED net power compared to baseline values

3.3 Comparision to Alternative Power Sources

RED's potential for future use as a supplemental power source for small mobile platforms is dependent on how it compares to alternative environmental energy harvesting methods and the duration of time needed to recharge a Li-ion battery. Additionally, it is important to understand the period of time at which a RED stack would be able to supply more sustained power than a comparable Li-ion battery. These metrics help to frame a greater understanding of the

technology's viability for small mobile platforms in specific geographic regions, such as the Artic and river estuaries.

The volumetric and specific power density of a system are valuable metrics by which to compare otherwise dissimilar energy systems. Using a mass of 3.15 kg for a 100 cell RED stack with 10 cm by 20 cm of active membrane area and a total volume 360 cm^2 and the optimum dimensions and concentrations previously calculated, the volumetric and specific energy density of a RED stack were found to be 2.35 W/kg and 206×10^{-3} W/cm^3 at 298K with salt concentrations of 0.7 and 35 g NaCl/ kg H_2O. Table 0.2 shows the mass distribution of the various components of the RED stack.

Table 0.2: Mass of 100 Cell RED Stack by Component

Component	Quantity	Mass (Kg)	Total (Kg)
Profiled CEM	101	0.004	0.404
Profiled AEM	100	0.003	0.300
Platinum Electrodes	2	0.023	0.046
Polymer Endplates	2	0.699	1.398
Screws and Bolts	1	1	1
100 Cell RED Stack	-	-	3.15

Figure 0-7 compares RED's volumetric and specific power densities with those of other environmental energy harvesters that directly produce electricity.
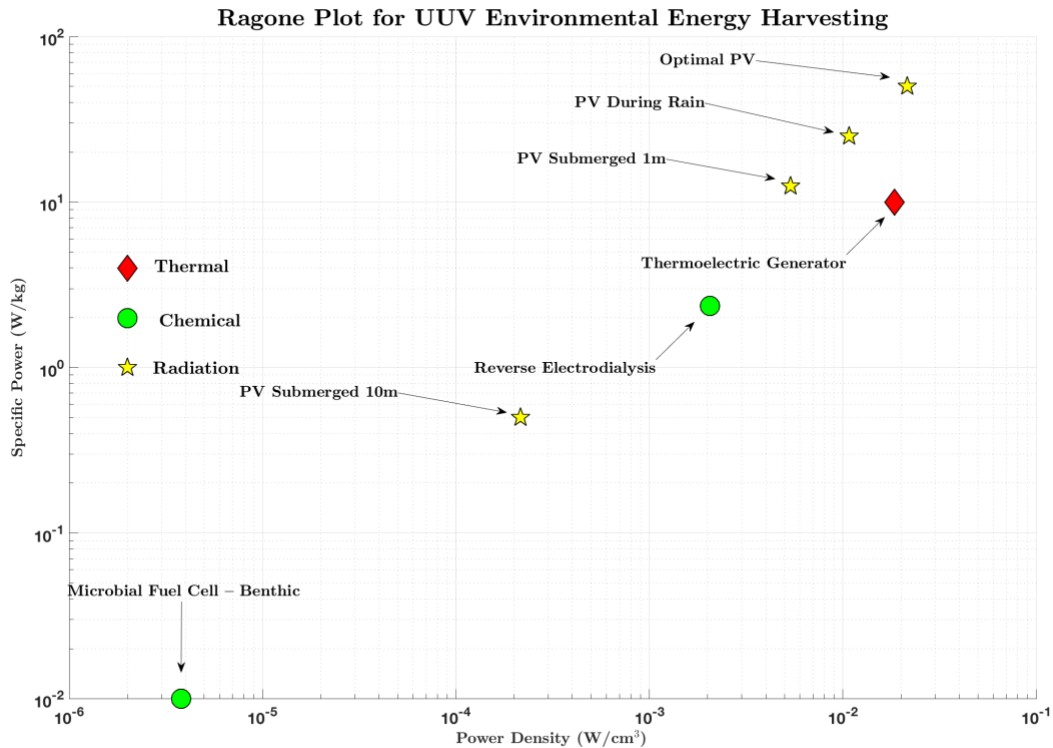
Figure 0-7: Volumetric and specific power density comparison between various environmental electrical energy harvesting devices that could be utilized by a moving system [65]–[67].

It can be seen that RED is roughly an order of magnitude smaller than most flexible photovoltaic (PV) alternatives on both a volumetric and specific basis. However, it is worth noting the massive drop in power density that PV experiences when submerged at increasingly great depths. At 10 meters below the surface PV's power densities decrease 2.5 orders of magnitude. In addition to the need to remain relatively close to the surface, photovoltaic cells are also not a viable option when travelling under ice, as is often found in the Arctic regions. Thermoelectric generators, which utilize the Seebeck effect to produce power, also have roughly an order of magnitude greater volumetric and specific energy densities than RED. Yet once again, the environmental constraints of the Arctic prove less than ideal for the system, as

thermoelectric generators require greater temperature gradients than found in the Arctic waters to produce substantial power. While lower temperatures do detrimentally affect the performance of RED, Figure 0-5 shows its viability even at low temperatures. Consequently, the Arctic offers a unique opportunity for the use of RED as a means to harvest energy.

However, current autonomous mobile platforms often utilize batteries, particularly lithium ion. With lithium ion batteries having volumetric and specific energy densities as high as 650 Wh/L and 250 Wh/kg [68], RED is not a viable replacement for the vast majority of scenarios. However, in certain situations it could be used as an supplemental means to recharge a battery, in effect creating discrete undersea charging stations. At optimal conditons, it would take an RED cell approximately 13.1 days to recharge a lithium ion battery of equivalent volume and 4.4 days for one of equivalent mass. While these are substantial durations of time, RED does provide an alterntive means of recharging the battery in challenging environments where few other viable alternatives exist.
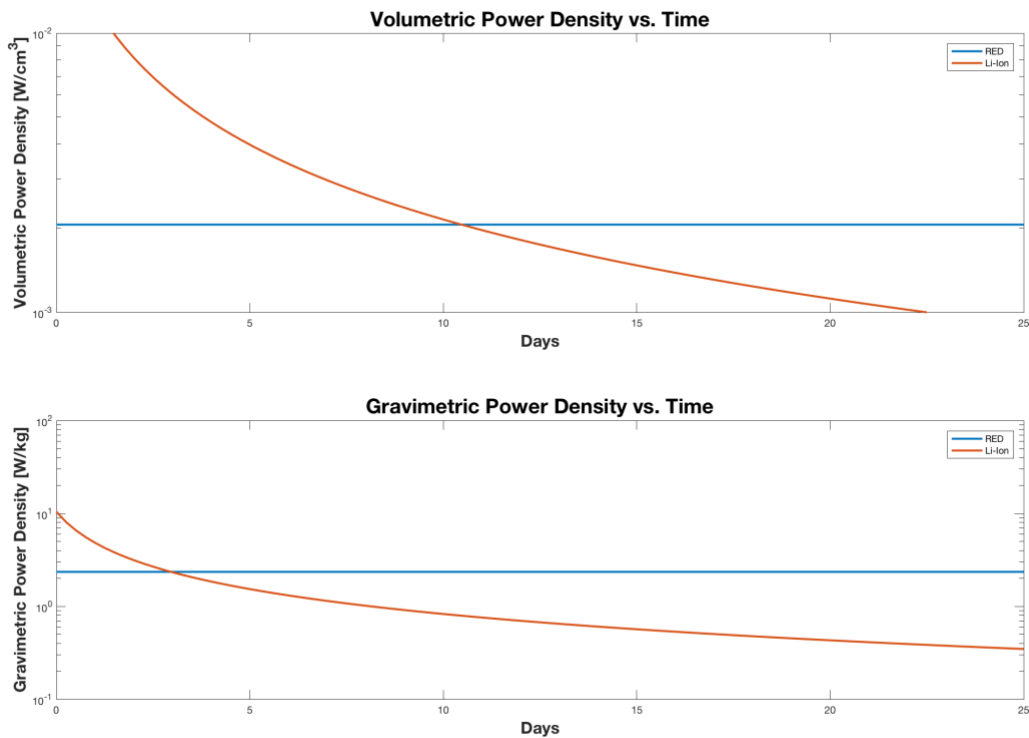
Figure 0-8: Comparison between lithium ion batteries and RED on a volumetric (top) and specific (bottom) power density basis. The point of intersection (approximately 10.4 days for the volumetric comparison and 3 days for the mass based) is the duration of time at which a RED cell would be able to provide the same energy to a system as a comparable volume or mass of lithium ion batteries.

In examining extremely low powered devices RED might serve as a viable power source. However, once again it must be assessed at what point lithium ion batteries would be more effective. Figure 0-8 compares the volumetric and specific power densities of a RED stack and a lithium ion battery of equal volume and mass over time. While RED has a constant specific and volumetric power density, that of lithium ion batteries is dependent on the duration of time. The point of intersection represents the period of time for which a RED stack and lithium ion battery would supply equal quantities of power to a small mobile platform. Past this point, RED would be able to provide a greater power supply.

THIS PAGE INTENTIONALLY LEFT BLANK

Chapter 4
Future Outlook and Conclusions

4.1 Future Outlook and Research

While it has been shown analytically that RED has potential for use in specific geographic regions, further work is needed to successfully construct an actual lightweight prototype RED cell. Empirical data from a lightweight prototype RED stack would also further substantiate the claims regarding RED's volumetric and specific energy densities. Ultimately, a full-scale prototype of the dimensions specified by the model should be built and tested.

With regards to modeling, better characterization of profiled membranes and their subsequent pumping losses could be improved. In particular, the models for the pumping losses differ from stack to stack, depending on the geometries of the stack and their spacer properties. A more comprehensive model would be extremely useful. Additionally, while gravimetric and volumetric assessments were made for a RED stack, further work should be done in assessing the RED system, specifically incorporating the mass and size of the required pumps, which do not scale linearly. Finally, more accurate mapping of the regions where RED could be effectively applied would be extremely useful. Gaining a more accurate grasp of the specific geographic regions where RED could be implemented would be useful for future analysis when planning what power sources to use for small-scale platforms.

4.2 Summary and Conclusion

A unique parameter sweep model was constructed from first order principles and some empirical data in order to find the optimal dimensions, flow rates, and concentrations in order to maximize the volumetric power density of a RED stack. Unlike past models, this model accounted for considerations unique to RED's application to unmanned underwater vehicles and remote sensing devices in variable environmental conditions. Additionally, the model maintained broad generality for use with a variety of RED design configurations, while also demonstrating agreement with empirical data collected from specific experimental tests. This model was then validated with experimental results reported by Veerman et al. [64], Vermaas et al. [35], and Güler et al. [39] before being used to identify optimal design properties. It was found that while the channel height had no effect on the power density, the ideal length was unbounded and approached zero, which was in agreement with previous literature [44]. Using 50^4 data points it was determined that the approximate optimal dimensions for a stack using profiled membranes were 53.2 μm and 81.5 μm and 3.91 cm/s and 7.54 cm/s for the dilute and concentrated channels respectively. This was specified for a RED stack with a fixed length of 10 cm and height of 20 cm using pillared profiled membranes oeprating at 25°C. The modified net power $P_{net,mod}$ per volume was then found to be 1.55×10^{-3} W/cm^3 and 206×10^{-3} W/cm^3 for temperatures of 4°C and 25°C respectively. Additionally, the specific power density at 25°C was calculated to be 2.35 W/kg.

Finally, RED was compared to other environmental energy harvesting system technologies and was found to have potential for specific uses in harsh environments, like the Arctic. In assessing the RED's potential as a supplemental power source to Li-ion batteries, it

was found that RED would only see viable use for longer duration missions, as it would take a RED stack over five days to recharge an equivalent mass of lithium ion batteries and over thirteen days for an equivalent volume. Furthermore, it was assessed that RED could only be used as the primary power source for extremely low power systems intended for missions spanning more than two days.

THIS PAGE INTENTIONALLY LEFT BLANK

Appendix A: Nomenclature

Nomenclature			
b	Width between profiled ridges	R_{stack}	RED Stack Resistance
C	Mass Concentration	r	Area Resistance
c	Molar Concentration	T	Temperature
d_H	Hydraulic Diameter	t_{res}	Residence Time
E	Energy	V_P	Displaced Volume
F	Faraday's Constant	V_W	Volume of Water
f	Darcy Friction Factor	V_{stack}	Voltage Across the RED Stack
ΔG_{mix}	Gibbs Free Energy of Mixing	v	Velocity
$\Delta G_{mix,V_A}$	Gibbs Free Energy of Mixing per Volume of Solution A	W	Work
h	Channel Height	w	Width or Intermembrane Distance
I_{stack}	Current Across the Stack	x	Mole Fraction
j	Current Density	y	Depth below the surface
k	Conductivity	z	Ion Valence
L	Channel Length	**Greek Symbols**	
M	Molecular Weight	α	Membrane Permselectivity
n_{cell}	Total number of cells	β	Spacer Masking Factor
$P_{buoyant}$	Power due to Buoyant Forces	γ	Activity Coefficient
P_{net}	Net Power	ε	Spacer Porosity
P_{pump}	Pumping Power	μ	Dynamic Viscosity
P_{stack}	Power Produced by the RED Stack	ρ	Density
Δp	Change in Pressure	υ	Number of Ions into which a Molecule Dissociates
S_{vsp}	Ratio of Spacer Surface Area to its Volume	ϕ	Mole Ratio
Q	Volumetric Flow Rate	**Subscripts**	
R_{gas}	Ideal Gas Constant	0	Reference State
R_{Bl}	Boundary Layer Resistance	A	Solution A
$R_{\Delta C}$	Resistance Due to the Concentration Drop Along the Channel	B	Solution B
R_{elec}	Electrode Resistance	H	High Concentration Solution
R_{load}	Load Resistance	L	Low Concentration Solution
R_{ohmic}	Ohmic Resistance	L	Low Concentration Solution

Appendix B: Pressure Drop Correction Factors

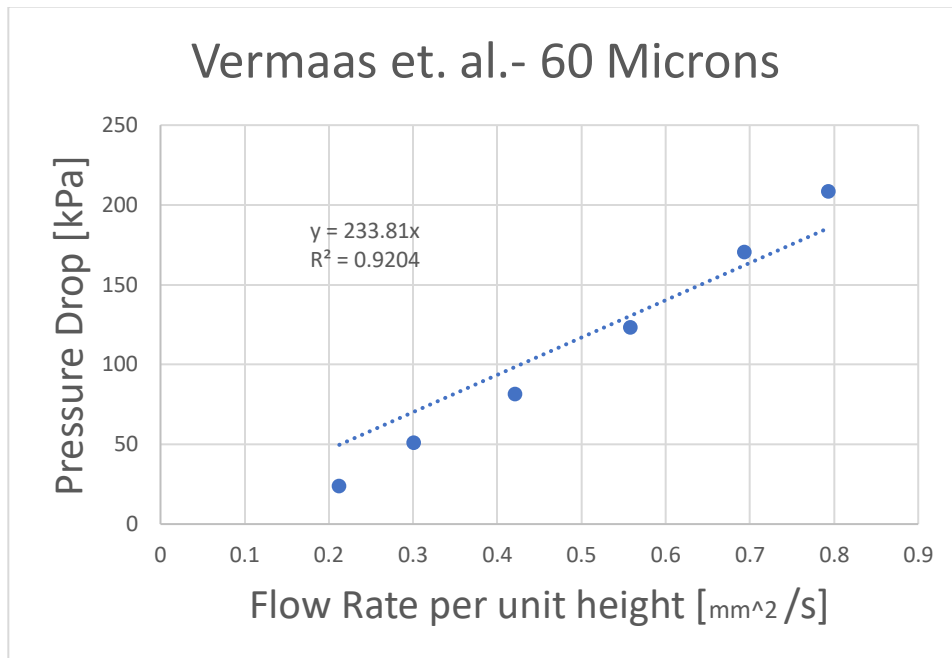Figure B-1: Pressure drop versus flow rate per unit height (mm^2/s) from Vermaas et al. [35] for a spacer-filled RED stack with an intermembrane width of 60 μm. The corresponding slope of the trendline was used as a correction factor for the pumping losses, as the pressure drop is linear with the flow velocity.

Figure B-2: Pressure drop versus flow rate per unit height (mm^2/s) from Vermaas et al. [35] for a RED stack with a nominal intermembrane width of 100 μm

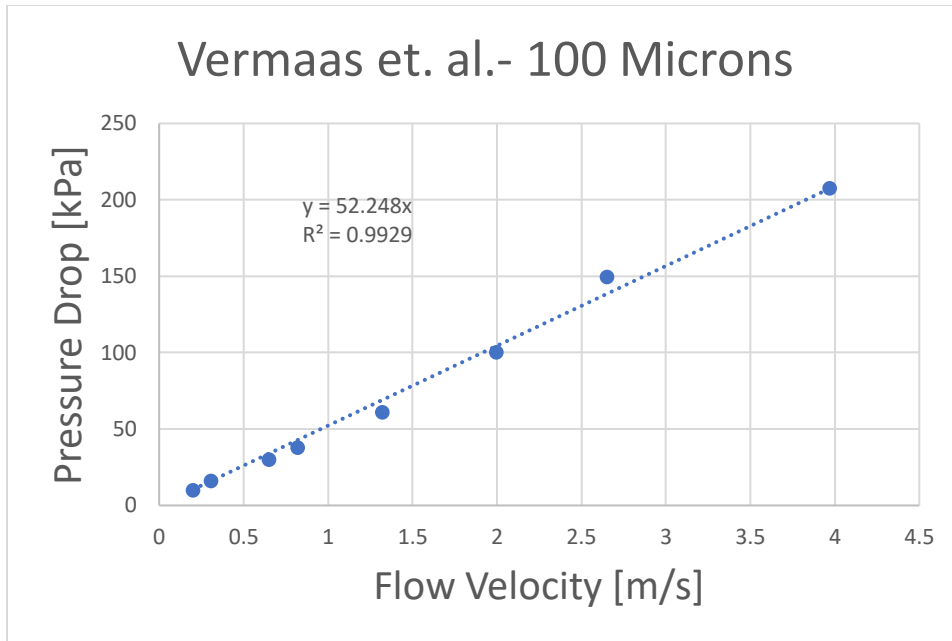

Figure B-3: Pressure drop versus flow rate per unit height (mm^2/s) from Vermaas et al. [35] for a RED stack with a nominal intermembrane width of 200 μm
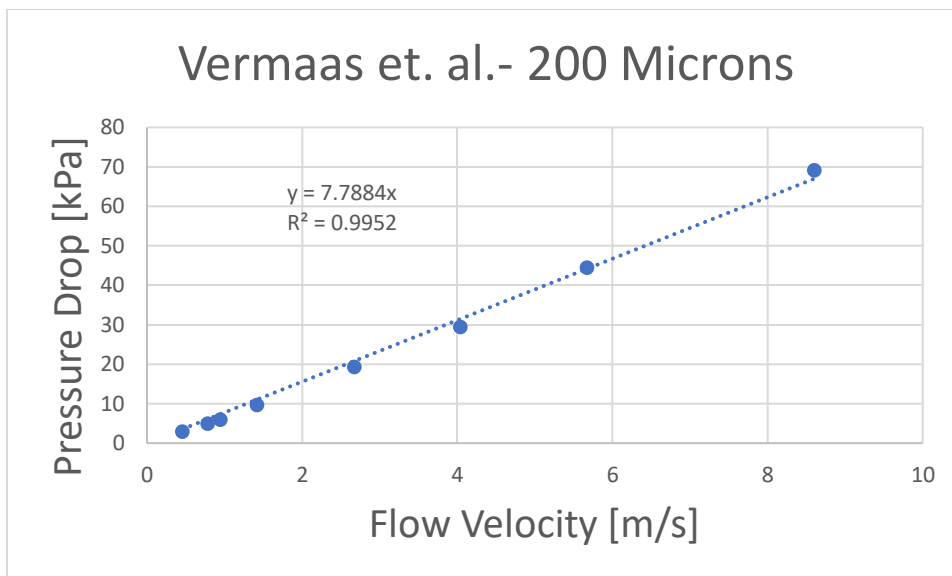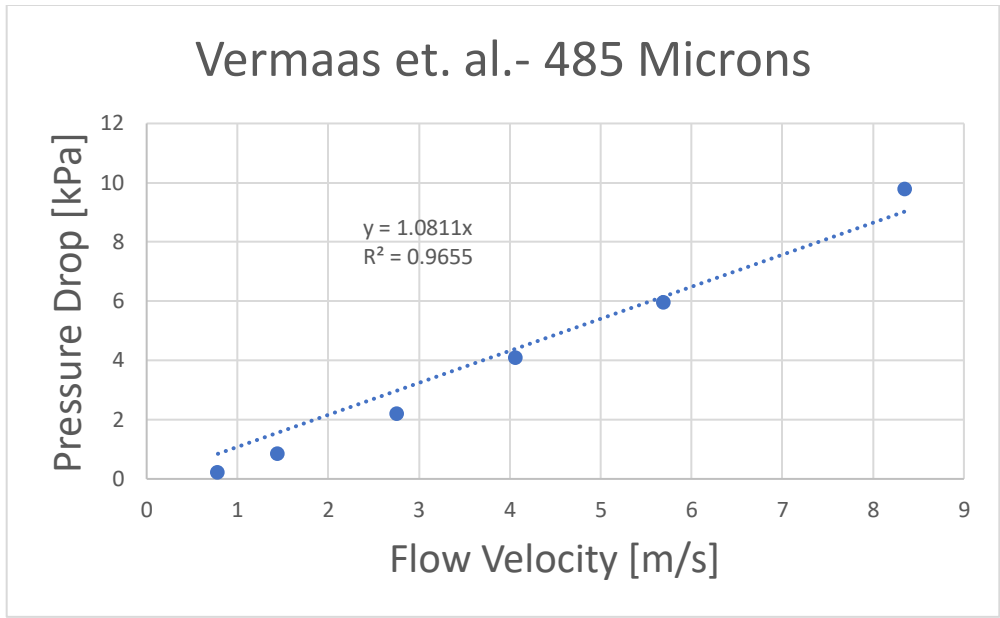
Figure B-4: Pressure drop versus flow rate per unit height (mm^2/s) from Vermaas et al. [35] for a RED stack with a nominal intermembrane width of 485 μm
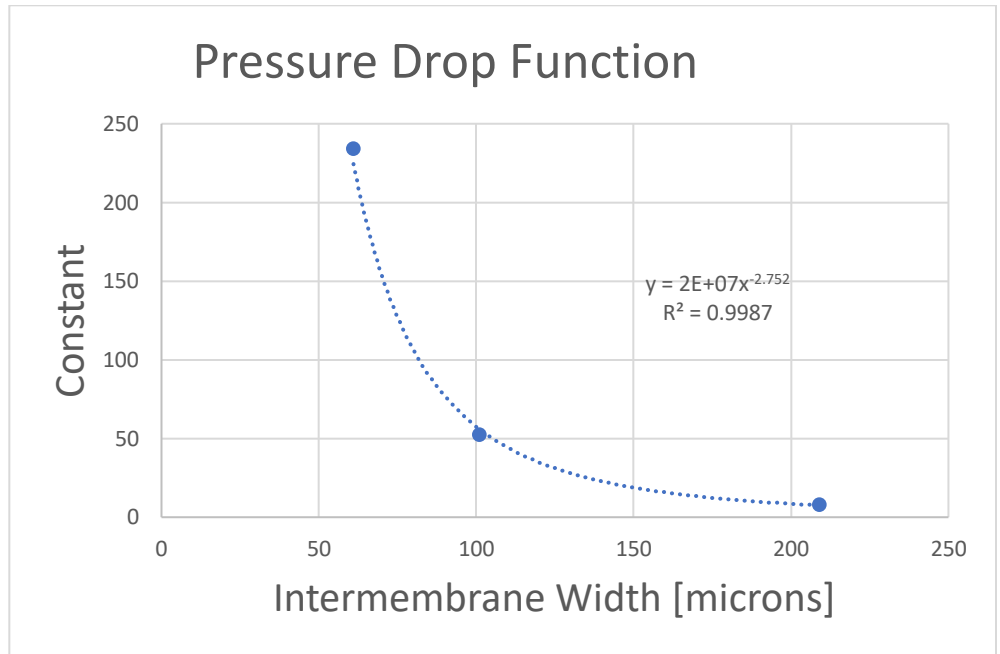
Figure B-5: Graph of the four slopes from the trendlines in Figures A-1 to A-4 versus the intermembrane width of the stack
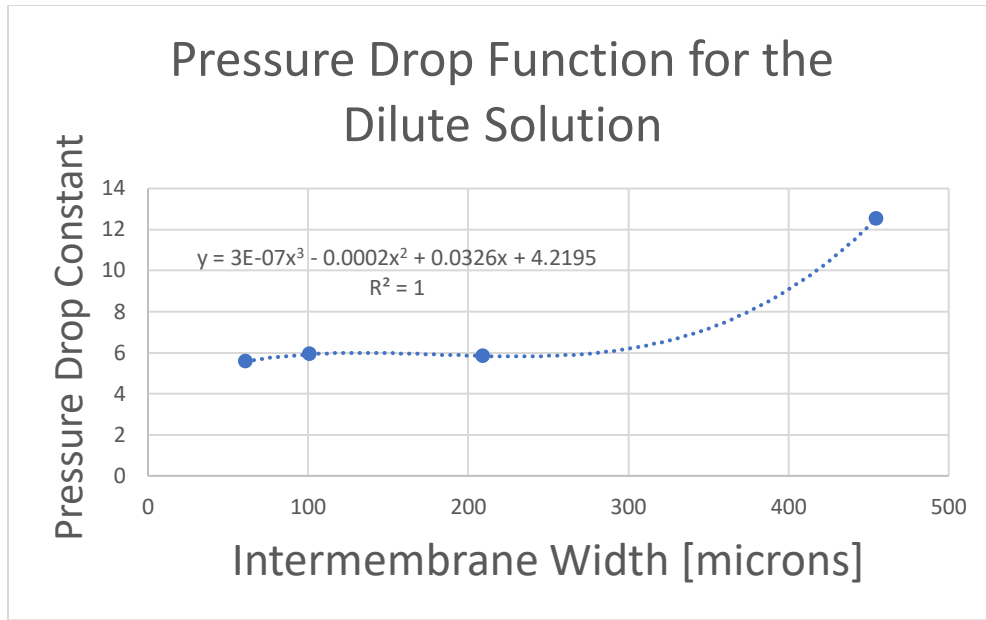
Figure B-6: Graph of the pumping loss constants for the dilute channel calculated from the constants in Figure A-5 and modified so as to be used with the Darcy-Weisbach equation. The resulting curve was used to predict the correction factor for the pumping loss of various RED stacks at intermembrane distances between 60 and 485μm.
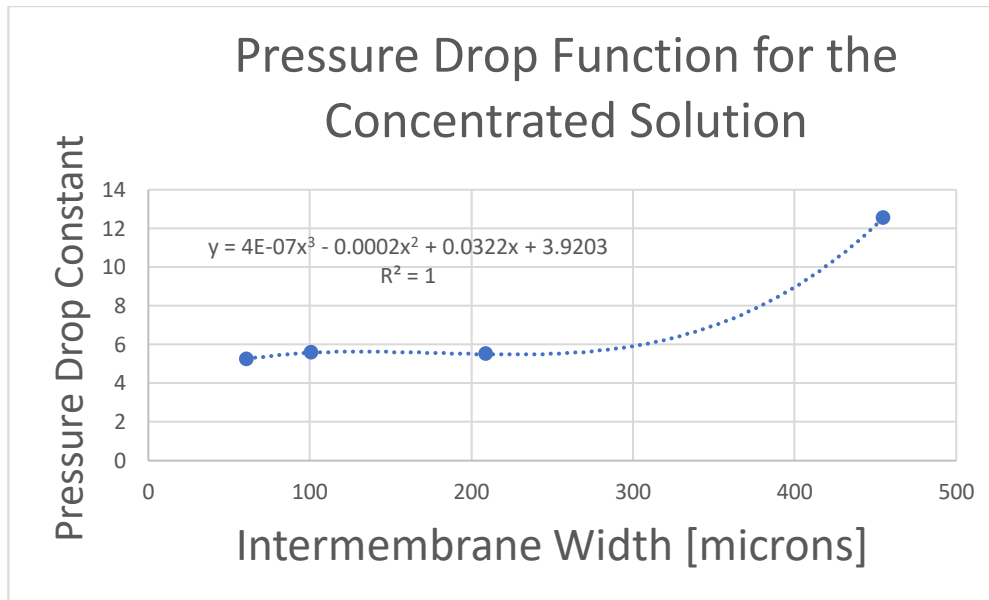
Figure B-7: Graph of the pumping loss constant for the concentrated channel calculated from the constant in Figure A-5 and modified so as to be used with the Darcy-Weisbach equation. The resulting curve was used to predict the correction factor for the pumping loss of various RED stacks at intermembrane distances between 60 and 485μm.
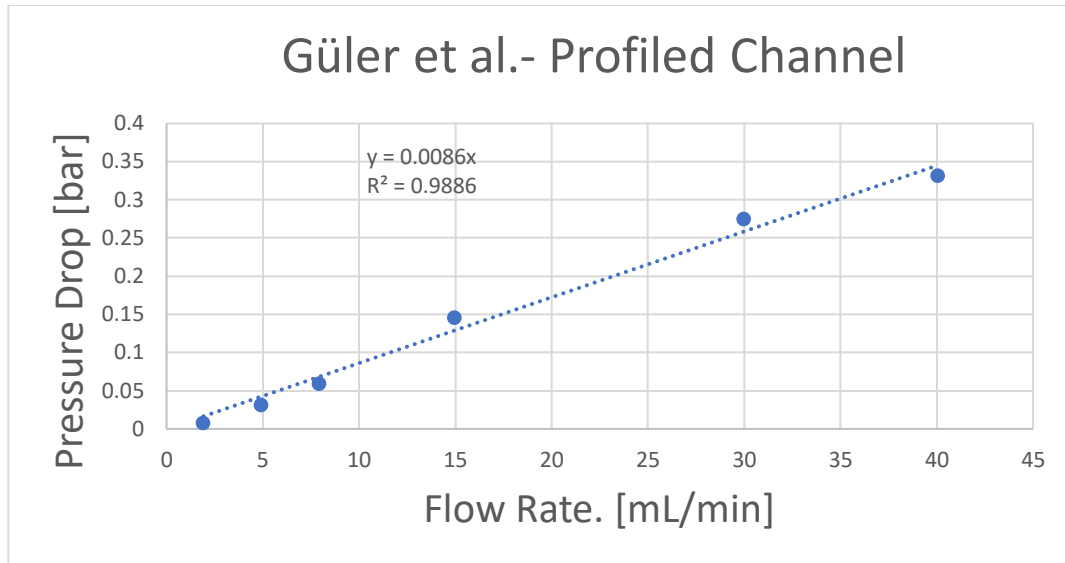
Figure B-8: Pressure Drop versus flow rate per unit height (mm^2/s) from Güler et al. [39] for a RED stack with profiled membranes at an intermembrane distance of 100μm. The corresponding slope of the trendline was used to derive a correction factor for Darcy-Weisbach equation for profiled channels.

Appendix C: Comparison between Computational Predictions and Empirical Data

RED Stacks with Spacer-Filled Channels

Figure C-1: Comparison between the model and empirical results for the total resistance per cell (top left), gross power per membrane area (top right), pressure drop along a channel (bottom left), and net power per membrane area (bottom right) produced by a five cell RED stack with nominal intermembrane widths of 60μm (61μm measured) [35]

Figure C-2: Comparison between the model and empirical results for the total resistance per cell (top left), gross power per membrane area (top right), pressure drop along a channel (bottom left), and net power per membrane area (bottom right) produced by a five cell RED stack with nominal intermembrane widths of 100μm (101μm measured) [35]
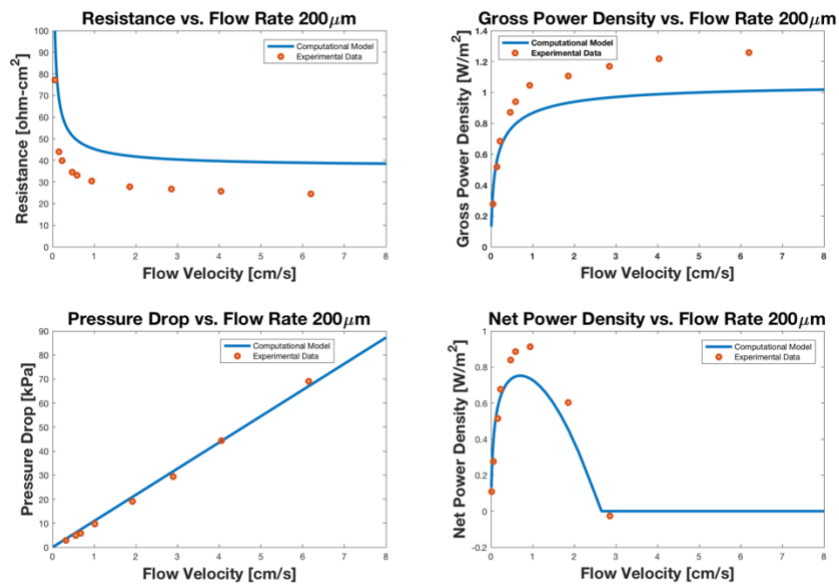
Figure C-3: Comparison between the model and empirical results for the total resistance per cell (top left), gross power per membrane area (top right), pressure drop along a channel (bottom left), and net power per membrane area (bottom right) produced by a five cell RED stack with nominal intermembrane widths of 200μm (209μm measured) [35]
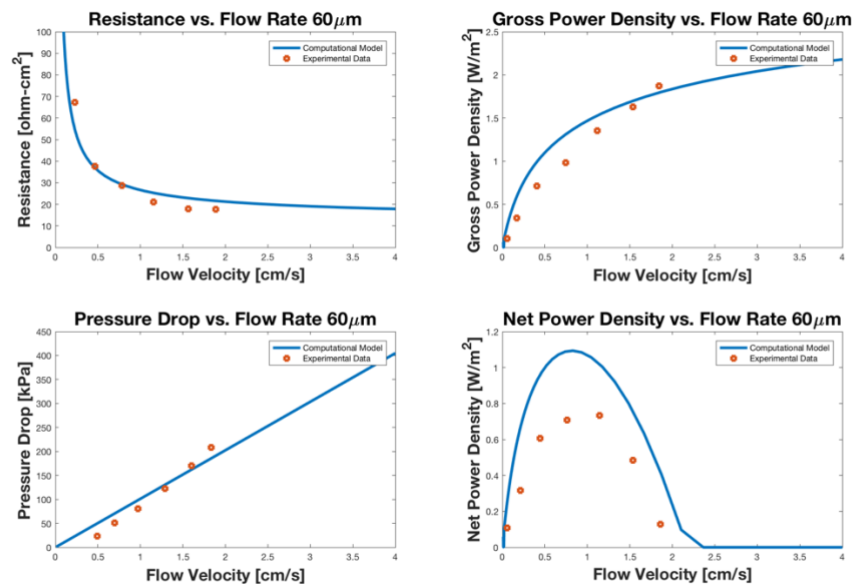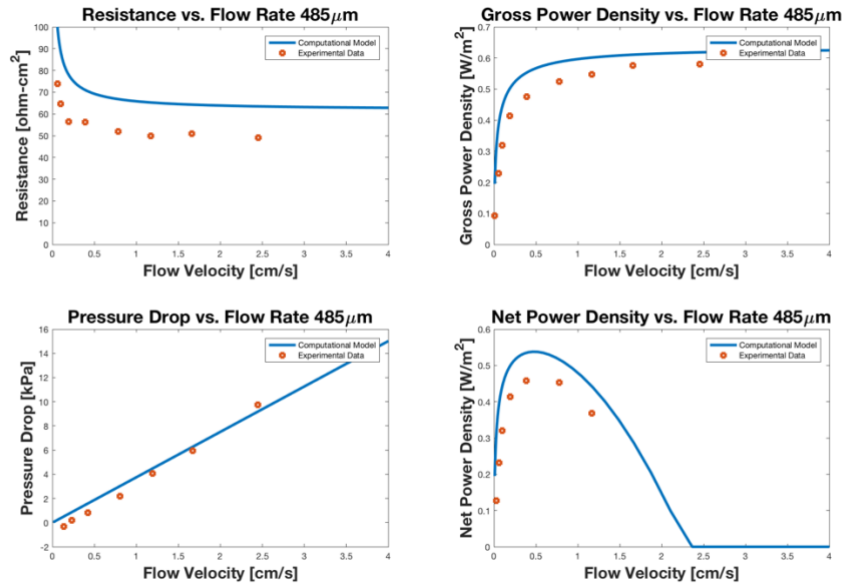
Figure C-4: Comparison between the model and empirical results for the total resistance per cell (top left), gross power per membrane area (top right), pressure drop along a channel (bottom left), and net power per membrane area (bottom right) produced by a five cell RED stack with nominal intermembrane widths of 485μm (455μm measured) [35]
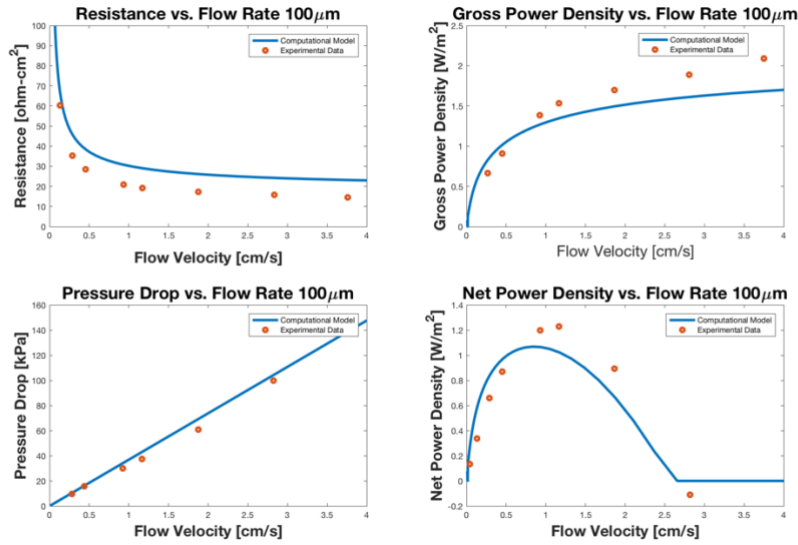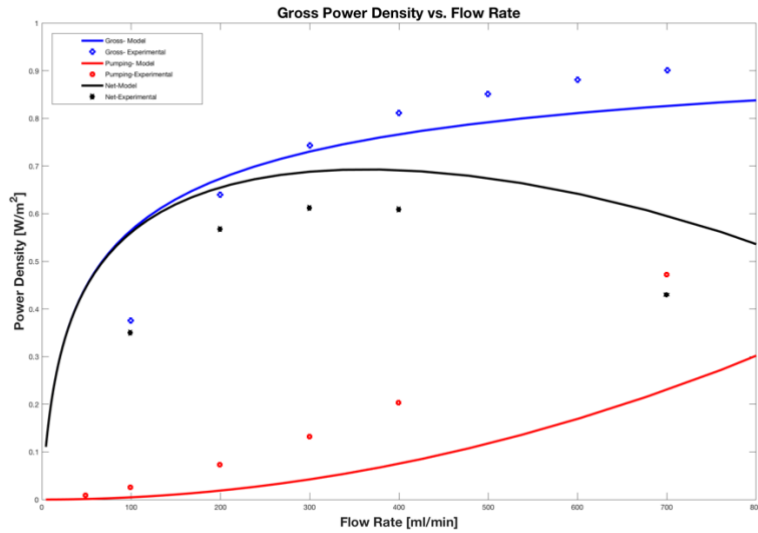

Figure C-5: Comparison between the model and empirical results for the gross power per membrane area, pumping power per membrane area, and net power per pumping area for a 50 cell RED stack with nominal spacing of 200μm [64]

RED Stacks with Profiled Membranes
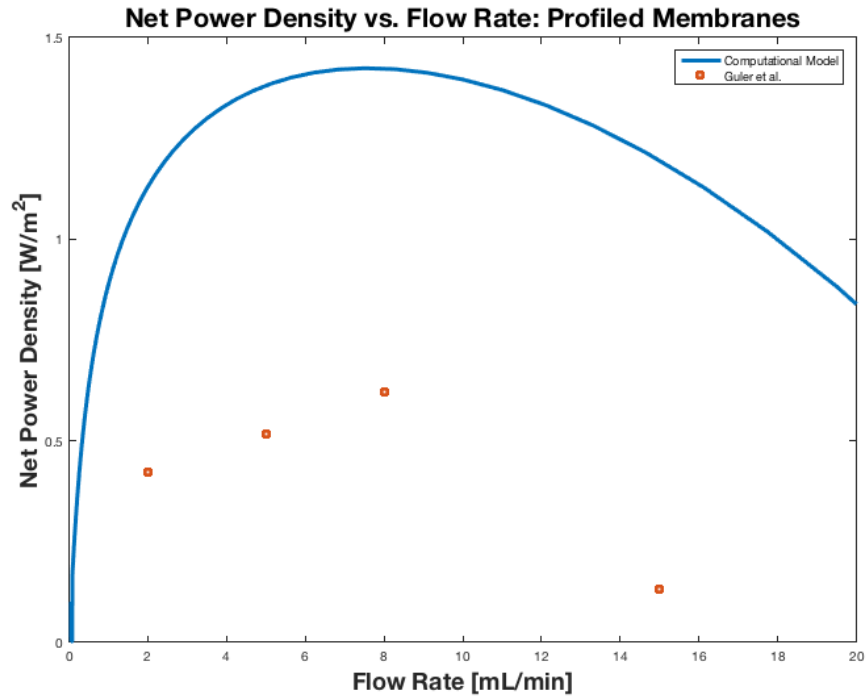
Figure C-6: Comparison between the model and empirical results for the net power per membrane area of a profiled channel in a two cell RED stack with nominal intermembrane widths of 100μm [39]

Appendix D: Temperature versus Pumping Power
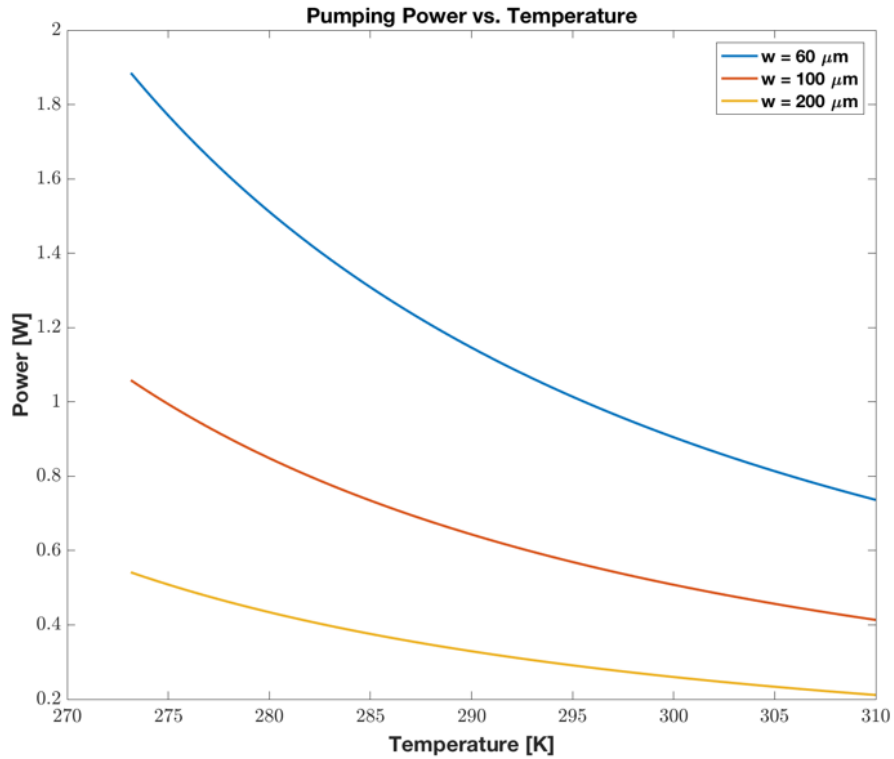
Figure D-1: Pumping power losses for RED stacks of various intermembrane widths as a function of temperature. The stacks' height and length are 10 cm respectively and the flow rate simulated is 1 cm/s. This graph illustrates the large role that temperature has in increasing the pumping losses for small channel stacks due to the sensitivity of water's dynamic viscosity to low temperatures.

Bibliography

[1]   N. Y. Yip and M. Elimelech, "Thermodynamic and Energy Efficiency Analysis of Power Generation from Natural Salinity Gradients by Pressure Retarded Osmosis," 2012.

[2]   J. D. Isaacs and R. J. Seymour, "The ocean as a power resource," *Int. J. Environ. Stud.*, vol. 4, no. 1–4, pp. 201–205, 1973.

[3]   G. L. Wick and W. R. Schmitt, "Prospects for Renewable Energy from the Sea," *Mar. Technol. Soc. J.*, vol. 11, no. 5–6, pp. 16–21, 1977.

[4]   G. Z. Ramon, B. J. Feinberg, and E. M. V. Hoek, "Membrane-based production of salinity-gradient power," *Energy Environ. Sci.*, vol. 4, no. 11, p. 4423, 2011.

[5]   R. E. Pattle, "Production of Electric Power by mixing Fresh and Salt Water in the Hydroelectric Pile," *Nature*, vol. 174, p. 660, 1954.

[6]   N. Y. Yip, D. Brogioli, H. V. M. Hamelers, and K. Nijmeijer, "Salinity Gradients for Sustainable Energy: Primer, Progress, and Prospects," *Environ. Sci. Technol.*, p. acs.est.6b03448, 2016.

[7]   F. Helfer, C. Lemckert, and Y. G. Anissimov, "Osmotic power with Pressure Retarded Osmosis: Theory, performance and trends - A review," *J. Memb. Sci.*, vol. 453, pp. 337–358, 2014.

[8]   S. E. Skilhagen, J. E. Dugstad, and R. J. Aaberg, "Osmotic power - power production based on the osmotic pressure difference between waters with varying salt gradients," *Desalination*, vol. 220, no. 1–3, pp. 476–482, 2008.

[9]   M. Tedesco, A. Cipollina, A. Tamburini, and G. Micale, "Towards 1 kW power production in a reverse electrodialysis pilot plant with saline waters and concentrated brines," *J. Memb. Sci.*, vol. 522, pp. 226–236, 2017.

[10]   A. M. Weiner, R. K. McGovern, and J. H. Lienhard V, "A new reverse electrodialysis design strategy which significantly reduces the levelized cost of electricity," *J. Memb. Sci.*, vol. 493, pp. 605–614, 2015.

[11]   D. Brogioli, "Extracting renewable energy from a salinity difference using a capacitor," *Phys. Rev. Lett.*, vol. 103, no. 5, pp. 31–34, 2009.

[12]   F. La Mantia, D. Brogioli, and M. Pasta, *Capacitive mixing and mixing entropy battery*. 2016.

[13]   F. Liu, O. Schaetzle, B. B. Sales, M. Saakes, C. J. N. Buisman, and H. V. M. Hamelers, "Effect of additional charging and current density on the performance of Capacitive energy extraction based on Donnan Potential," *Energy Environ. Sci.*, vol. 5, no. 9, p. 8642, 2012.

[14]   S. Loeb and R. S. Norman, "Osmotic Power Plants," *Science*, vol. 189, no. 4203, pp. 654–655, 1975.

[15]   S. Zhang, G. Han, X. Li, and C. Wan, *Pressure retarded osmosis: Fundamentals*. 2016.

[16] N. Y. Yip and M. Elimelech, "Comparison of energy efficiency and power density in pressure retarded osmosis and reverse electrodialysis," *Environ. Sci. Technol.*, vol. 48, no. 18, pp. 11002–11012, 2014.

[17] D. (Statkraft) Heinisch, "Statkraft PRO Power Plant in Tofte, Norway." National Geographic, 2013.

[18] G. Griffiths, J. Jamieson, S. Mitchell, and K. Rutherford, "Energy storage for long endurance AUVs," *Adv. Technol. Underw. Veh.*, pp. 8–16, 2004.

[19] R. E. Pattle, "Electricity from fresh and salt water- Without fuel," *Chem. Process Eng.*, vol. 35, pp. 351–354, 1955.

[20] G. W. Murphy and R. R. Matthews, "Osmionic demineralization.," *Industrial & Engineering Chemistry (1923)*, vol. 50. pp. 1181–1188, Aug-1958.

[21] G. W. Murphy and R. R. Matthews, "Migration in transference cells with and without membranes—application to osmionic demineralization," *Electrochim. Acta*, vol. 12, no. 8, pp. 983–998, Jan. 1967.

[22] R. E. Lacey, C. E. Feazel, E. W. Lang, A. Southern Research Institute (Birmingham, and U. S. O. of S. Water., "Development." U.S. Dept. of the Interior, 1960.

[23] J. Veerman and D. A. Vermaas, *Reverse electrodialysis: Fundamentals*. Elsevier Ltd., 2016.

[24] J. N. Weinstein and F. B. Leitz, "Electric power from differences in salinity: the dialytic battery.," *Science*, vol. 191, no. 3, pp. 557–559, 1976.

[25] R. E. Lacey, "Energy by reverse electrodialysis," *Ocean Eng.*, vol. 7, no. 1, pp. 1–47, 1980.

[26] V. Kniajev, "Energy of salinity gradient - new source of energy with minimal environmental impact. Kniajev V.," in *International Workshop "Result of Fundamental Research for Investments*, 2001.

[27] J. W. Post, "Blue Energy: electricity production from salinity gradients by reverse electrodialysis," Wageningen University, 2009.

[28] P. E. Dlugolecki, "Mass transport in reverse electrodialysis for sustainable energy generation," University of Twente, 2009.

[29] J. Veerman, "Reverse electrodialysis: design and optimization by modeling and experimentation," University of Groningen, 2010.

[30] E. Guler, "Anion exchange membrane design for reverse electrodialysis," University Twente, 2014.

[31] D. A. Vermaas, "Energy generation from mixing salt water and fresh water: smart flow strategies for reverse electrodialysis," University Twente, 2014.

[32] B. E. Logan and M. Elimelech, "Membrane-based processes for sustainable power generation using water," *Nature*, vol. 488, no. 7411, pp. 313–319, 2012.

[33] D. A. Vermaas, J. Veerman, N. Y. Yip, M. Elimelech, M. Saakes, and K. Nijmeijer, "High

Efficiency in Energy Generation from Salinity Gradients with Reverse Electrodialysis," *ACS Sustain. Chem. Eng.*, vol. 1, pp. 1295–1302, 2013.

[34]   N. Y. Yip, D. A. Vermaas, K. Nijmeijer, and M. Elimelech, "Thermodynamic, Energy Efficiency, and Power Density Analysis of Reverse Electrodialysis Power Generation with Natural Salinity Gradients," *Environ. Sci. Technol.*, vol. 48, pp. 4925–4936, 2014.

[35]   D. A. Vermaas, M. Saakes, and K. Nijmeijer, "Doubled Power Density from Salinity Gradients at Reduced Intermembrane Distance," *Environ. Sci. Technol.*, vol. 45, no. 16, pp. 7089–7095, Aug. 2011.

[36]   A. Daniilidis, D. A. Vermaas, R. Herber, and K. Nijmeijer, "Experimentally obtainable energy from mixing river water, seawater or brines with reverse electrodialysis," *Renew. Energy*, vol. 64, pp. 123–131, 2014.

[37]   E. Güler, R. Elizen, D. A. Vermaas, M. Saakes, and K. Nijmeijer, "Performance-determining membrane properties in reverse electrodialysis," *J. Memb. Sci.*, vol. 446, pp. 266–276, 2013.

[38]   D. A. Vermaas, M. Saakes, and K. Nijmeijer, "Power generation using profiled membranes in reverse electrodialysis," *J. Memb. Sci.*, vol. 385–386, pp. 234–242, 2011.

[39]   E. Güler, R. Elizen, M. Saakes, and K. Nijmeijer, "Micro-structured membranes for electricity generation by reverse electrodialysis," *J. Memb. Sci.*, vol. 458, pp. 136–148, 2014.

[40]   S. Pawlowski, T. Rijnaarts, M. Saakes, K. Nijmeijer, J. G. Crespo, and S. Velizarov, "Improved fluid mixing and power density in reverse electrodialysis stacks with chevron-profiled membranes," *J. Memb. Sci.*, vol. 531, no. November 2016, pp. 111–121, 2017.

[41]   S. Pawlowski, V. Geraldes, J. G. Crespo, and S. Velizarov, "Computational fluid dynamics (CFD) assisted analysis of profiled membranes performance in reverse electrodialysis," *J. Memb. Sci.*, vol. 502, pp. 179–190, 2016.

[42]   D. A. Vermaas, J. Veerman, and K. Nijmeijer, "Influence of multivalent ions on renewable energy generation in reverse electrodialysis," *Energy Environ. Sci.*, vol. 7, pp. 1434–1445, 2014.

[43]   J. Veerman, M. Saakes, S. J. Metz, and G. J. A. N. Harmsen, "Electrical Power from Sea and River Water by Reverse Electrodialysis: A First Step from the Laboratory to a Real Power Plant," *Environ. Sci. Technol.*, vol. 44, no. 23, pp. 9207–9212, 2010.

[44]   J. Veerman, M. Saakes, S. J. Metz, and G. J. Harmsen, "Reverse electrodialysis: A validated process model for design and optimization," *Chem. Eng. J.*, vol. 166, pp. 256–268, 2011.

[45]   A. Cipollina *et al.*, *Reverse electrodialysis: Applications*. Elsevier Ltd., 2016.

[46]   Reds. B.V., "REDstack," 2018.

[47]   M. R. Carnes, "Description and Evaluation of GDEM-V 3.0," Stennis Space Center, MS, 2009.

[48] US Navy Climate Change Task Force, "USN Arctic Roadmap 2014-2030," Washington D.C., 2014.

[49] I. Sudakov, S. A. Vakulenko, and K. M. Golden, "Arctic melt ponds and bifurcations in the climate system," *Commun. Nonlinear Sci. Numer. Simul.*, vol. 22, no. 1–3, pp. 70–81, 2015.

[50] J. a. Richter-Menge, D. K. Perovich, and W. Scott Pegau, "Summer ice dynamics during SHEBA and its effect on the ocean heat content," *Ann. Glaciol.*, vol. 33, no. October 1997, pp. 201–206, 2001.

[51] U.S. Navy, "The Navy Unmanned Undersea Vehicle (UUV) Master Plan," 2004. [Online]. Available: http://www.navy.mil/navydata/technology/uuvmp.pdf.

[52] J. D. Stachiw, "Performance of Photovoltaic Cells in Undersea Environment," *J. Eng. Ind.*, vol. 102, no. 1, p. 51, 1980.

[53] M. W. Shafer and E. Morgan, "Energy Harvesting for Marine-Wildlife Monitoring," in *SMASIS2014*, 2014, no. 46155, p. V002T07A017.

[54] D. A. Vermaas, E. Guler, M. Saakes, and K. Nijmeijer, "Theoretical power density from salinity gradients using reverse electrodialysis," *Energy Procedia*, vol. 20, pp. 170–184, 2012.

[55] J. Veerman, J. W. Post, M. Saakes, S. J. Metz, and G. J. Harmsen, "Reducing power losses caused by ionic shortcut currents in reverse electrodialysis stacks by a validated model," *J. Memb. Sci.*, vol. 310, no. 1–2, pp. 418–430, 2008.

[56] D. A. Vermaas, D. Kunteng, M. Saakes, and K. Nijmeijer, "Fouling in reverse electrodialysis under natural conditions," *Water Res.*, vol. 47, no. 3, pp. 1289–1298, 2013.

[57] D. A. Vermaas, D. Kunteng, J. Veerman, M. Saakes, and K. Nijmeijer, "Periodic feedwater reversal and air sparging as antifouling strategies in reverse electrodialysis," *Environ. Sci. Technol.*, vol. 48, no. 5, pp. 3065–3073, 2014.

[58] M. Vaselbehagh, H. Karkhanechi, R. Takagi, and H. Matsuyama, "Biofouling phenomena on anion exchange membranes under the reverse electrodialysis process," *J. Memb. Sci.*, vol. 530, no. November 2016, pp. 232–239, 2017.

[59] P. M. Page, "Flow in pipes," in *Fluid Mechanics*, pp. 321–343.

[60] A. Miquel and G. Schock, "Mass transfer and pressure loss in spiral wound modules," *Desalination*, vol. 64, no. 1–3, p. 339, Oct. 1987.

[61] A. R. Da Costa, A. G. Fane, and D. E. Wiley, "Spacer characterization and pressure drop modelling in spacer-filled channels for ultrafiltration," *J. Memb. Sci.*, vol. 87, pp. 79–98, Jan. 1994.

[62] M. H. Sharqawy, J. H. Lienhard V, and S. M. Zubair, "The thermophysical properties of seawater: A review of existing correlations and data Accessed Thermophysical properties of seawater: A review of existing correlations and data," *Desalin. Water Treat.*, vol. 16, no. August 2015, pp. 354–380, 2010.

[63] K. G. Nayar, M. H. Sharqawy, L. D. Banchik, and J. H. Lienhard, "Thermophysical properties of seawater: A review and new correlations that include pressure dependence," *Desalination*, vol. 390, pp. 1–24, 2016.

[64] J. Veerman, M. Saakes, S. J. Metz, and G. J. Harmsen, "Reverse electrodialysis: Performance of a stack with 50 cells on the mixing of sea and river water," *J. Memb. Sci.*, vol. 327, no. 1–2, pp. 136–144, 2009.

[65] Thermal Electronics Corp, "Thermoelectric Power Modules 190C for Liquid to Liquid Apps," 2016. [Online]. Available: https://tecteg.com/thermoelectric-power-modules-190c-375f-for-liquid-to-liquid-apps/. [Accessed: 11-May-2018].

[66] S. Surampudi, "Overview of the Space Power Conversion and Energy Storage Technologies," Pasadena, 2011.

[67] M. E. Nielsen, C. E. Reimers, and H. A. Stecher, "Enhanced power from chambered benthic microbial fuel cells," *Environ. Sci. Technol.*, vol. 41, no. 22, pp. 7895–7900, 2007.

[68] A. Manthiram, "An Outlook on Lithium Ion Battery Technology," *ACS Cent. Sci.*, vol. 3, no. 10, pp. 1063–1069, 2017.